

Population synthesis of exocometary gas around A stars

S. Marino^{1*}, M. Flock¹, Th. Henning¹, Q. Kral², L. Matrà³ and M. C. Wyatt⁴

¹Max Planck Institute for Astronomy, Königstuhl 17, 69117 Heidelberg, Germany

²LESIA, Observatoire de Paris, Université PSL, CNRS, Sorbonne Université, Univ. Paris Diderot, Sorbonne Paris Cité, 5 place Jules Janssen, 92

³Harvard-Smithsonian Center for Astrophysics, 60 Garden Street, Cambridge, MA 02138, USA

⁴Institute of Astronomy, University of Cambridge, Madingley Road, Cambridge CB3 0HA, UK

Accepted XXX. Received YYY; in original form ZZZ

ABSTRACT

The presence of CO gas around 10-50 Myr old A stars with debris discs has sparked debate on whether the gas is primordial or secondary. Since secondary gas released from planetesimals is poor in H₂, it was thought that CO would quickly photodissociate never reaching the high levels observed around the majority of A stars with bright debris discs. Kral et al. (2019) showed that neutral carbon produced by CO photodissociation can effectively shield CO and potentially explain the high CO masses around 9 A stars with bright debris discs. Here we present a new model that simulates the gas viscous evolution, accounting for carbon shielding and how the gas release rate decreases with time as the planetesimal disc loses mass. We find that the present gas mass in a system is highly dependant on its evolutionary path. Since gas is lost on long timescales, it can retain a memory of the initial disc mass. Moreover, we find that gas levels can be out of equilibrium and quickly evolving from a shielded onto an unshielded state. With this model, we build the first population synthesis of gas around A stars, which we use to constrain the disc viscosity. We find a good match with a high viscosity ($\alpha \sim 0.1$), indicating that gas is lost on timescales $\sim 1 - 10$ Myr. Moreover, our model also shows that high CO masses are not expected around FGK stars since their planetesimal discs are born with lower masses, explaining why shielded discs are only found around A stars. Finally, we hypothesise that the observed carbon cavities could be due to radiation pressure or accreting planets.

Key words: circumstellar matter - planetary systems - accretion discs - methods: numerical.

1 INTRODUCTION

The discovery of circumstellar gas around young main-sequence stars with debris discs dates back more than two decades, with a few systems showing molecular emission at millimetre wavelengths (e.g. Zuckerman et al. 1995) and others atomic absorption in the UV (Slettebak 1975), some of which varies with time (Ferlet et al. 1987). Thanks to Herschel, it also became possible to study the gas component in the far-IR through atomic emission from ionised carbon and neutral oxygen (e.g. Riviere-Marichalar et al. 2012; Roberge et al. 2013; Cataldi et al. 2014), adding a third tool for the observational study of gas in systems with debris discs. Today we know of about 20 systems with debris discs and gas detected in emission, and another ~ 11 systems (with and without infrared excess) with circumstellar gas detected in

absorption only (e.g. Montgomery & Welsh 2012; Welsh & Montgomery 2018; Rebollido et al. 2018; Iglesias et al. 2018).

While there has been some consensus on the origin of the absorption lines as arising from *falling evaporating bodies* (FEBs, Ferlet et al. 1987; Beust et al. 1990; Beust & Morbidelli 1996; Kiefer et al. 2014), no model has been completely successful at explaining the colder emitting gas at tens of au that is now found around ~ 20 systems (e.g. Moór et al. 2011; Dent et al. 2014; Moór et al. 2015; Marino et al. 2016; Greaves et al. 2016; Lieman-Sifry et al. 2016; Marino et al. 2017; Matrà et al. 2017b; Moór et al. 2017; Matrà et al. 2019), mostly through CO detections. Since CO molecules exposed to stellar and interstellar UV radiation will photodissociate in short-timescales ($\lesssim 120$ yr, Hudson 1971; van Dishoeck & Black 1988; Visser et al. 2009), the CO detected in some of these systems suggests that we are observing these systems at a very particular moment (e.g. at the later stages of protoplanetary disc dispersal, hereafter primordial

* E-mail: sebastian.marino.estay@gmail.com

origin) or CO and other gas species are being replenished in these systems (hereafter secondary origin). [Zuckerman & Song \(2012\)](#) proposed that gas could be released in the same collisional cascade that replenishes the dust levels in debris discs. The amount of gas and dust, could then be used to infer the volatile composition of planetesimals. This scenario would be consistent with systems with the low CO levels observed, for example, around β Pic, HD 181327 and Fomalhaut. However, a significant fraction of the systems with detected CO would require planetesimals much richer in CO and/or CO₂ compared to Solar System comets, or gas release rates that are decoupled from the inferred dust production rates ([Kral et al. 2017](#)). Furthermore, the systems with the highest CO content have ages between 10-50 Myr and their content is not necessarily correlated with their debris disc-like dust ([Moór et al. 2017](#)). Therefore, these have been tagged as *hybrid discs* meaning they have primordial gas leftovers and secondary dust ([Kóspál et al. 2013](#)), although it is not clear how primordial gas has survived for so long in those systems.

A potential pathway to alleviate these tensions in the secondary origin scenario, is that the CO becomes shielded from UV radiation in systems with high gas content and its lifetime is much longer than in the unshielded case. While debris discs are optically thin hence dust cannot effectively shield the gas, CO can become self-shielded or shielded by molecular hydrogen ([van Dishoeck & Black 1988](#); [Visser et al. 2009](#)). This is difficult since H₂ is unlikely to be present at high densities in this secondary origin scenario, and CO would need to be released at a very high rate to reach the necessary column densities to become self-shielded ([Kral et al. 2017](#)). However, carbon that is produced through CO photodissociation can also shield CO from UV photons, becoming ionised ([Rollins & Rawlings 2012](#)). Carbon and oxygen are expected to viscously evolve and form an atomic accretion disc ([Kral et al. 2016](#)), even if the stellar luminosity is high enough to blow out carbon since it can remain bound due to self-shielding and interactions with more bound species such as oxygen ([Fernández et al. 2006](#); [Kral et al. 2017](#)). [Kral et al. \(2019\)](#) found that if viscosities were low or the CO input rate high, enough carbon could accumulate to shield CO and explain hybrid discs as shielded discs of secondary origin.

So far, none of the above studies has considered the viscous evolution of an exocometary gas disc coupled with the time dependent gas release rate. If the release of gas is regulated by the mass loss rate in the planetesimal disc, then we expect this to decrease steeply with time relaxing into a collisional equilibrium (e.g. [Dominik & Decin 2003](#); [Krivov et al. 2006](#); [Wyatt et al. 2007a](#)). This means that the total gas mass input into a system depends strongly on its previous evolution if the gas lifetime is similar or longer than the age of the system (or collisional timescales). If viscosities are low, this could well be the case for shielded discs, thus collisional evolution cannot be neglected a priori. In this paper we consider the effect of an evolving mass input rate on the viscous evolution of the gas in the system, particularly we focus on CO and carbon. This paper is structured as follows. We first present our model and numerical simulations in §2. Then in §3 we use this model to produce a population synthesis of A stars with debris discs that release gas, which we compare with observations. In §4 we show that

the same model applied to FGK stars is also consistent with observations. In §5 we discuss our results and some of our assumptions, and finally in §6 we report our conclusions.

2 MODEL

The gas evolution is treated with a simple viscous evolution 1D model, focusing only on the radial dimension and assuming axisymmetry (similar to [Moór et al. 2019](#)). In this model, gas is input into the system at the radial locations of the planetesimal belt, from where it is allowed to viscously evolve. The gas surface density evolution, Σ_G , is then set by the usual viscous evolution equation ([Lynden-Bell & Pringle 1974](#)) with the addition of an input source that arises from a collisional cascade of planetesimals, $\dot{\Sigma}_{\text{coll}}^+(r, t)$,

$$\frac{\partial \Sigma_G}{\partial t} = \frac{3}{r} \frac{\partial}{\partial r} \left[r^{1/2} \frac{\partial}{\partial r} (\nu \Sigma_G r^{1/2}) \right] + \dot{\Sigma}_{\text{coll}}^+(r, t), \quad (1)$$

where ν is the kinematic viscosity. In Equation 1, we have also made the usual approximation that the orbital velocity does not significantly differ from circular Keplerian rotation.

Rather than studying Σ_G , in this paper we are mainly interested in following the evolution of CO, C and O, which can have significantly different distributions ([Kral et al. 2016](#)). Therefore, instead of solving Equation 1, we solve for the evolution of the surface density of each gas species Σ_i by advecting its mass at the viscous radial velocity, v_r , hence

$$\frac{\partial \Sigma_i}{\partial t} = -\frac{1}{r} \frac{\partial}{\partial r} (r v_r \Sigma_i) + \dot{\Sigma}_i^\pm(r, t), \quad (2)$$

$$\Sigma_G v_r = -\frac{3}{\sqrt{r}} \frac{\partial}{\partial r} (\nu \Sigma_G \sqrt{r}), \quad (3)$$

$$\Sigma_G = \sum_i \Sigma_i \quad (4)$$

where $\dot{\Sigma}_i^\pm(r, t)$ represents the additional production and destruction processes (e.g. CO photodissociation, see below) and v_r the radial velocity of the gas. Equation 2 is a continuity equation with a source term, while Equation 3 is the conservation of angular momentum which is applicable to the total mass. We solve Equations 2 and 3 using first-order explicit finite-volume update following [Bath & Pringle \(1981\)](#) and [Booth et al. \(2017\)](#). We also include the diffusion of the gas species, that is given by

$$\frac{\partial f_i}{\partial t} = \frac{1}{r \Sigma_G} \left(r \nu \Sigma_G \frac{\partial f_i}{\partial r} \right), \quad (5)$$

where $f_i = \Sigma_i / \Sigma_G$ and we have taken a Schmidt number of unity ([Stevenson 1990](#); [Turner et al. 2006](#)). The addition of Equation 5 accounts for the diffusion due to turbulent mixing rather than an accretion flow. It does not affect the total surface density, but the relative abundances of CO, carbon and oxygen.

For the viscosity we make the standard assumption of an alpha disc model, with $\nu = \alpha c_s^2 / \Omega_K$, where c_s is the sound speed and Ω_K the Keplerian speed. The sound speed is calculated from the gas temperature, which is fixed and taken equal to the blackbody temperature for simplicity ($T = 278 L_\star^{1/4} r^{-1/2}$) and a mean-molecular weight that can vary between 28 and 14 depending on if the gas is dominated by CO or by atomic oxygen and carbon. This choice

of parametrization of ν is arbitrary, but it offers a form simple enough to understand the gas evolution. Note that we expect α to be smaller than unity, although its value has only been constrained between $10^{-4} - 0.5$ (Kral et al. 2016; Kral & Latter 2016; Kral et al. 2019; Moór et al. 2019).

The input of gas in the system happens through the release of volatile species that escape after the break up of volatile rich bodies in a collisional cascade. This release is spatially confined to a planetesimal belt that extends in radius and is radially resolved by our simulations. Furthermore, we assume that the released gas is completely dominated by CO. In principle, other molecular species such as CO₂, H₂O, HCN, etc. could also be released, however, current observations are roughly consistent with CO dominated gas release. The addition of other gas species is discussed in §5.1.1.

Once CO is released and exposed to interstellar UV radiation it will photodissociate into carbon and oxygen on a short timescale of 120 yr (Visser et al. 2009), or even shorter depending on the strength of the stellar UV flux (Matrà et al. 2017a). For example, a stellar luminosity higher than $20 L_{\odot}$ will shorten the CO photodissociation timescale to less than 10 year within ~ 100 au if unshielded (see Figure 1 in Kral et al. 2017). This timescale, however, can be much longer if the CO column densities are high enough to shield itself or if neutral carbon is present. The latter is of special interest since depending on how fast CO is released and carbon viscously spreads, it could explain the existence of large amounts of CO in 10–50 Myr old systems (Kral et al. 2019).

In this work we will focus solely on the effect of interstellar UV radiation and will neglect the stellar contribution. This is justified by the two following reasons. First, most of the discs that we want to explain have stellar luminosities below $20 L_{\odot}$ and debris disc sizes of ~ 100 au, which means that if CO was completely unshielded its lifetime would be of 120 yr and dominated by ISRF. Second, the column densities of CO and carbon along the radial direction will be 1–5 orders of magnitude larger than in the vertical direction because the radial distribution of gas is typically much broader than the disc scale height. This means that CO will be highly shielded in the radial direction (see estimates in § 5.1.3). Therefore, UV interstellar radiation from the top and bottom of the disc will be the predominant factor that sets the CO lifetime.

Then, $\dot{\Sigma}_i^{+,-}(r, t)$ for CO and C/O becomes (Kral et al. 2019)

$$\dot{\Sigma}_{\text{CO}}^{\pm}(r, t) = \dot{\Sigma}_{\text{CO}}^{+} - \frac{\Sigma_{\text{CO}}}{T_{\text{ph}}(\Sigma_{\text{CO}}, \Sigma_{\text{C}})}, \quad (6)$$

$$\dot{\Sigma}_{\text{C}}^{\pm}(r, t) = +\frac{3}{7} \frac{\Sigma_{\text{CO}}}{T_{\text{ph}}(\Sigma_{\text{CO}}, \Sigma_{\text{C}})}, \quad (7)$$

$$T_{\text{ph}}(\Sigma_{\text{CO}}, \Sigma_{\text{C}}) = 120 \text{ yr} \frac{\exp[\Sigma_{\text{C}}/\Sigma_{\text{C}}^{\text{c}}]}{\Theta(\Sigma_{\text{CO}})}, \quad (8)$$

where $\dot{\Sigma}_{\text{CO}}^{+}$ is the input rate of CO and T_{ph} is the photodissociation timescale of CO which depends both on the column or surface density of CO (self-shielding) and neutral carbon C. The self-shielding function Θ is calculated by interpolating tabulated values in Visser et al. (2009, Table 6). This has a power-law-like dependence, with the CO lifetime increased by a factor of 2.7 when the average column density is 10^{15} cm^{-2} or a surface density of $4 \times 10^{-9} M_{\oplus} \text{ au}^{-2}$

($1.1 \times 10^{-7} \text{ g cm}^{-2}$). On the other hand, shielding by neutral carbon has an exponential dependence (Rollins & Rawlings 2012), with a critical surface density $\Sigma_{\text{C}}^{\text{c}} = 10^{-7} M_{\oplus} \text{ au}^{-2}$ ($2.7 \times 10^{-6} \text{ g cm}^{-2}$). A caveat in the calculation of T_{ph} is that in reality it will depend on the amount of material along every line of sight since the 120 yr reference lifetime assumes radiation is coming from all directions, therefore the *average* CO lifetime is expected to be slightly longer depending on the disc scale height.

Our model has two further simplifications. First, we consider that the ionisation fraction of carbon is negligible, or at least that the fraction of neutral carbon is not much lower than unity for discs in which neutral carbon plays an important role (this assumption is discussed in §5.1.2). Second, we neglect the stellar radiation pressure acting on carbon. In principle, neutral carbon could be blown out by radiation pressure for stellar luminosities greater than $\sim 20 L_{\odot}$ (Fernández et al. 2006, note that the specific threshold depends on the model spectrum used). This, however, probably does not happen in the discs we typically observe since even with a thousandth of the CO input rate estimated in β Pic, carbon is continuously produced and can reach densities that are high enough to become self-shielded from stellar UV and stay bound to the system (Kral et al. 2017). The effect of radiation pressure on carbon is further discussed in §5.3 and §5.5.

Finally, we consider the following boundary conditions. We use an inner radius of 1 au and we set $\nu_{\text{in}}\Sigma_{\text{G},\text{in}} = \text{const}$, such that the accretion rate is constant between the inner two cells and $\Sigma_{\text{G}}(r)$ tends to the expected solution that is inversely proportional to $\nu(r)$. For the surface density at the outer edge of our simulations (r_{out}), we take whichever is smaller between a power-law extrapolation or $\nu_{\text{out}}\Sigma_{\text{G},\text{out}} = \text{const}$. We find that when the CO mass input rate is constant, $r_{\text{out}} = 30r_{\text{belt}}$ is large enough and solutions converge. However, for CO mass input rates varying in time (§2.2) we find that convergence between solutions is achieved when r_{out} is a few times larger than the viscous characteristic radius ($r_{\text{belt}}(1+t/t_{\nu})$), thus we set $r_{\text{out}} = 3r_{\text{belt}}(1+t/t_{\nu})$, where t_{f} and t_{ν} are the length of the simulation and viscous timescale at r_{belt} ($t_{\nu} = r_{\text{belt}}^2/\nu(r_{\text{belt}})$). This ensures that the result from our simulations are not sensitive to the outer boundary conditions.

2.1 Constant CO input rate

Consider a disc of planetesimals around a $2 M_{\odot}$ ($16 L_{\odot}$) star, sustaining a collisional cascade that releases both dust and CO gas. Let's assume that CO is released at a constant rate $\dot{\Sigma}_{\text{CO}}^{+}$, parametrized as a Gaussian centred on $r_{\text{belt}} = 100$ au (belt mid radius) and with FWHM $\Delta r_{\text{belt}} = 50$ au. These are arbitrary choices, but overall consistent with the observed distribution of planetesimal disc radii and width around high luminosity stars (Matrà et al. 2018b). In Figure 1 the resulting evolution of the CO (left panels) and carbon (middle panels) surface densities and total masses (right panels) are shown for different CO mass input rates and values of α : 0.1 and 0.001. Hereafter we will refer to these α 's and resulting viscosities as high and low, respectively.

The top panel shows a simple case that would be applicable to systems that are observed to have a low CO gas

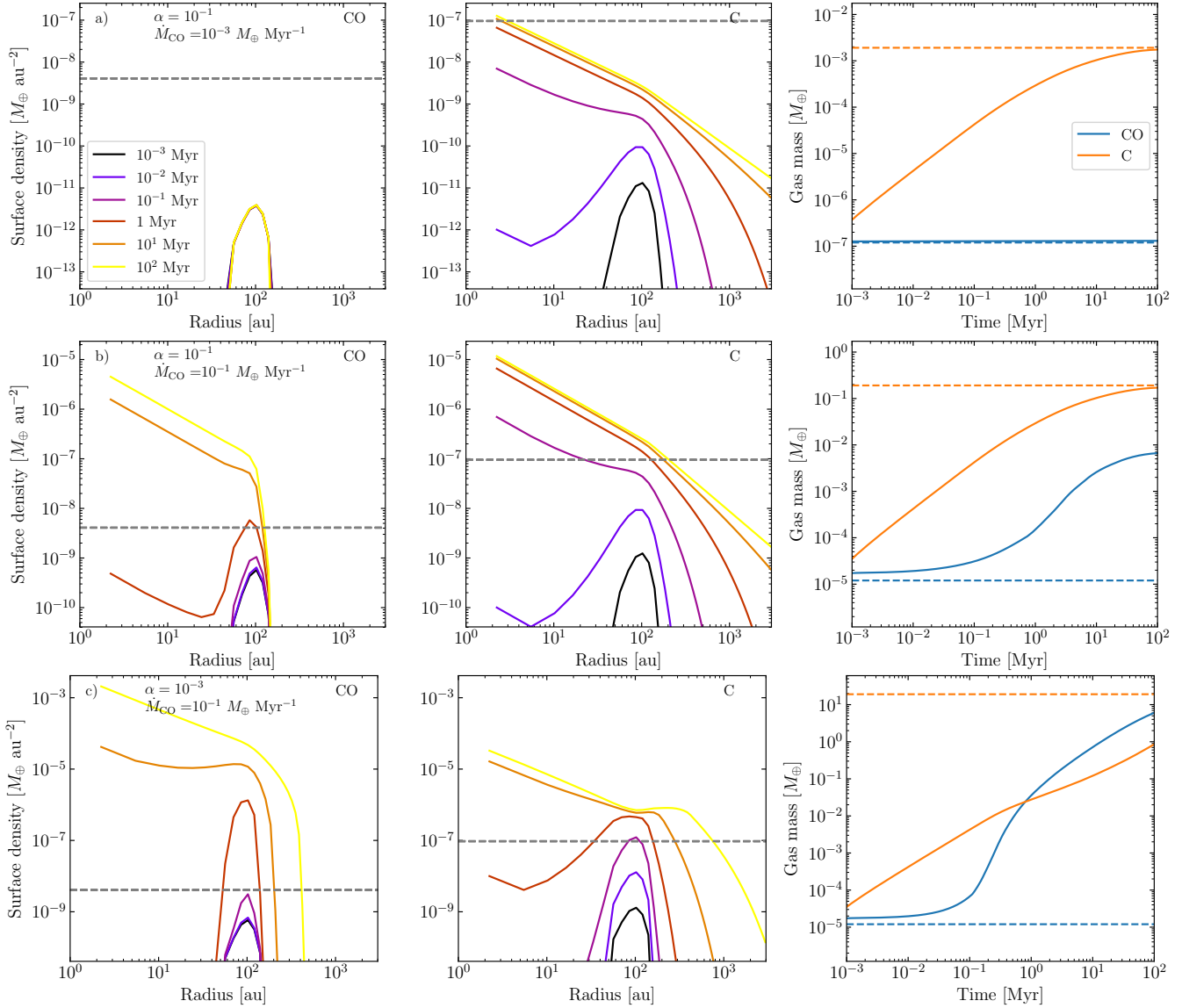


Figure 1. Viscous evolution of a gaseous disc over 100 Myr, with a constant input rate of CO over time and released roughly between 75–125 au, for three different cases. **Top:** high viscosity and low CO input rate. **Middle:** high viscosity and high CO input rate. **Bottom:** low viscosity and high CO input rate. The left and middle columns show the evolution of the CO and carbon surface density, respectively. The right column shows the evolution of the total gas mass of CO (blue continuous line) and carbon (orange continuous line). The dashed blue and orange lines represent the CO and carbon mass expected in steady state when CO is unshielded and the mass input rate of CO is constant over time.

mass (e.g. β Pic, HD 181327 and Fomalhaut, Dent et al. 2014; Marino et al. 2016; Matrà et al. 2017b). CO is input in the system and in a few hundred years it reaches steady state with $\Sigma_{\text{CO}} = \dot{\Sigma}_{\text{CO}}^+ \times 120 \text{ yrs}$ and thus is confined in space and co-located with planetesimals and large dust grains (top left). Carbon instead viscously spreads forming an accretion disc which reaches a steady state in a few times the viscous timescale at the belt location ($t_{\nu} = r_{\text{belt}}^2/\nu = 0.6 \text{ Myr}$, top middle). Neither the surface density of CO nor C reach the necessary levels to shield CO (grey dashed lines), except for carbon within a few AU where no CO is present. The final CO and C mass (top right) are consistent with analytic predictions where $M_{\text{CO}} = \dot{M}_{\text{CO}} \times 120 \text{ yrs}$ and M_{C} calculated by integrating equation B17 in Metzger et al. (2012) assuming that the viscosity scales linearly with radius (true for our

case if μ is constant),

$$M_{\text{C}} = \frac{2\dot{M}_{\text{CO}}r_{\text{belt}}^2}{7\nu_{\text{belt}}} \left[2 \left(\frac{r_{\text{max}}}{r_{\text{belt}}} \right)^{1/2} - 1 \right] \quad (9)$$

where r_{max} is the maximum radius in the simulation. Note that $M_{\text{C}} \propto r_{\text{max}}^{1/2}$, thus the total mass reported here is dominated by low density gas at large radii to which observations can be less sensitive. Therefore the carbon masses reported in this section cannot be compared directly with observations. Later in §3 we report instead the CO and carbon masses within 500 au which is a more sensible estimate to compare with typical observations. Note that if the viscosity did not scale linearly with radius, then the bulk of the mass could reside at small radii.

In the middle panels, the CO mass input rate is now 100 times higher. While the CO is slightly self-shielded within the first 0.1 Myr of evolution (note that the blue line in the right panel is above the dashed line), by 1 Myr the surface density of carbon reaches the critical level to shield CO at 100 au. The subsequent evolution has CO viscously spreading inwards forming an accretion disc and slightly diffusing outwards, although it is truncated at ~ 170 au where the CO lifetime becomes much shorter than the viscous timescale. Over time the carbon mass increases similarly to the upper panel, although the carbon mass saturates at a slightly lower level than the theoretical maximum because some of the CO is never photodissociated into carbon and oxygen ($\sim 15\%$).

In the lower panels we show a case with a low viscosity and high CO mass input rate. Due to the lower viscosity, carbon is locally piling up and so reaching a higher surface density much faster than it can spread out. By 0.1 Myr CO becomes shielded by carbon and starts to build up and viscously spread. With CO's significantly longer lifetime, the production rate of carbon is much lower, and the mass of CO overcomes the carbon mass after 1 Myr. Nevertheless, the carbon surface density is still comparable to the high viscosity case near the belt location, but orders of magnitude larger beyond 100 au. This means that CO can also significantly spread outwards since it is shielded out to 1000 au, although the viscous timescale to reach those regions can be shorter than its lifetime. Given the longer viscous timescale at r_{belt} (60 Myr), only by the end of the simulation the surface density of CO and carbon are close to steady state at the belt location. Something worth noticing in this last scenario is that the surface density of carbon after 10 Myr has a flat slope in between from r_{belt} out to where the CO surface density drops exponentially. In the two cases where CO becomes shielded, we find that CO spreads inwards reaching our simulation boundary at 1 au, and spreads outwards out to a radius where its lifetime against photodissociation (determined by both carbon and CO surface densities) is too short for CO to viscously spread or diffuse from where it is produced.

The CO and carbon evolution presented here is overall consistent with the 0D model presented in Kral et al. (2019, see their Figure 18). The main difference is that the predicted masses of carbon and CO (when completely shielded) are overall larger in this study for the same α since in Kral et al. (2019) we used the *local* viscous timescale which is a twelfth of the viscous timescale. Moreover, here we are considering the total gas mass in the system, which can be orders of magnitude higher than the gas mass around the belt location. Therefore, the disc mass saturates at a lower level in our previous simulations and in a shorter timescale.

2.2 Collisional evolution

An important ingredient that so far has not been considered in previous gas evolution studies (e.g. Kral et al. 2016, 2017, 2019) is the disc collisional evolution. These have assumed that CO gas is released at a constant rate equal to the product between the CO mass fraction in planetesimals, f_{CO} , and the mass loss rate due to collisions \dot{M} . While the first might stay constant overtime if planetesimals do not devolatise, the second typically decreases with time (e.g. Dominik & Decin 2003; Krivov et al. 2006; Wyatt et al. 2007a; Thébault &

Augereau 2007; Löhne et al. 2008; Kral et al. 2013) as planetesimals are ground down and mass is removed from the system through the blow out of small grains (Burns et al. 1979). Since the rate at which planetesimals suffer disruptive collisions is proportional to the total disc mass, M , it is easy to show that when assuming a single slope size distribution the disc mass should decrease with time as $1/t$, with

$$M(t) = \frac{M_0}{t/t_c + 1}, \quad (10)$$

$$\dot{M}(t) = -\frac{M(t)^2}{M_0 t_c}, \quad (11)$$

where t_c is the collisional lifetime of the largest planetesimals at $t = 0$ and M_0 is the initial disc mass. Note that t here represents the time since planetesimals were stirred enough to cause catastrophic collisions. Here we assume debris discs are pre-stirred and collisions start immediately after the protoplanetary disc is dispersed.

These equations have two strong implications for the evolution of the disc mass. First, for $t \gg t_c$ the disc mass will be simply proportional to $1/t$ and independent of M_0 . Thus two systems could have similar masses today although one started its evolution with a much higher disc mass than the other. Therefore the total gas mass released into the system over time can be orders of magnitude different depending on the initial conditions. Second, the mass loss rate decreases as t^{-2} , which is much faster than the $t^{-1/2}$ and $t^{-3/2}$ expected for the total mass and surface density of a gaseous disc that evolves viscously according to Equation 1 (without input sources). This means that the amount of gas in a debris disc can be out of equilibrium given its current gas release rate which has been decreasing with time.

The collisional lifetime is a function of the initial disc mass and other parameters such as the planetesimal strength, Q_D^* , maximum planetesimal size, D_c , mean eccentricity, e , mean inclination, I , disc mean radius, r , and width, dr . More generally, t_c is given by (Wyatt et al. 2007b)¹

$$t_c = \frac{3.8\rho r^{7/2}(dr/r)D_c}{M_\star^{1/2}M} \frac{8}{9G(X_c, q)}, \quad (12)$$

in years, where ρ is the internal density of solids in kg m^{-3} , r and dr are units of au, D_c is in units of km, M_\star is in units of M_\odot . $G(X_c, q)$ is a factor defined by Equation 10 in Wyatt et al. (2007b) that is a function of q (mass distribution exponent, $N(m) \propto m^{-q}$) and $X_c = D_{\text{cc}}/D_c$, with D_{cc} as the size of the smallest planetesimal that has sufficient energy to destroy a planetesimal of size D_c . Its value depends on the relative velocities and Q_D^* , and can be written as (Wyatt & Dent 2002)

$$X_c = 1.3 \times 10^{-3} \left(\frac{Q_D^* r M_\star^{-1}}{1.25e^2 + I^2} \right)^{1/3}, \quad (13)$$

with Q_D^* in units of J kg^{-1} . Assuming $\rho = 2700 \text{ kg m}^{-3}$, $I = e$ and $X_c \ll 1$, $q = 11/6$, then $G \approx 6.5 \times 10^6 [Q_D^* r / (M_\star e^2)]^{-5/6}$ and t_c can be written more simply as

$$t_c = 1.4 \times 10^{-9} r^{13/3} (dr/r) D_c Q_D^{5/6} e^{-5/3} M^{-1} M_\star^{-4/3}, \quad (14)$$

¹ Note that there is a typo in Wyatt et al. (2007b)'s equation as it should be in years rather than Myr

which is the same as Equation 16 in Wyatt (2008).

We use Equation 12 to calculate t_c and $\dot{M}(t)$ assuming an internal density of 2700 kg cm^{-3} , a maximum planetesimal size $D_c = 1 \text{ km}$, eccentricities and inclinations of 0.1, Q_D^* of 330 J kg^{-1} , $q = 11/6$ (i.e. a size distribution with a power law index of -3.5) and a fractional disc width of 0.5. Note that this particular choice of parameters is arbitrary, but in §3 we will fix these parameters to those chosen in Wyatt et al. (2007b) to fit the infrared excess evolution at 24 and $70 \mu\text{m}$ in nearby A stars (Rieke et al. 2005; Su et al. 2006), which are the focus of this paper. Finally, we assume a CO mass fraction in planetesimals of 0.1, consistent with levels inferred in Solar System comets (Mumma & Charnley 2011). Using this set of parameters, below we study the evolution of CO and carbon when the initial planetesimal disc mass is 300 or $30 M_\oplus$ ($t_c = 2$ and 20 Myr , respectively), and assuming $\alpha = 0.1$ (§2.2.1) and 10^{-3} (§2.2.2). This choice of masses is arbitrary, but it helps to illustrate how important the collisional evolution can be for the gas evolution.

2.2.1 High α

In Figure 2 we show the gas evolution for two discs starting with a total mass of 300 and $30 M_\oplus$ (10% of which is in CO) in the high viscosity case. In the high initial mass case (top panel), CO becomes self-shielded before carbon reaches the critical mass since the initial mass loss rate and CO mass input rate are very high ($\dot{M}_{\text{CO}} \sim 20 M_\oplus \text{ Myr}^{-1}$). Both CO and carbon viscously spread within 0.1 Myr, with carbon reaching larger radii, but not high enough surface densities to shield CO at radii larger than 500 au. For this initial mass, $t_c = 2 \text{ Myr}$, hence the evolution after a few Myr is characterised by a declining CO mass input rate ($1/t^2$) which cannot support anymore the high CO surface densities reached at $t = 1 \text{ Myr}$ since the lifetime of CO at the belt location is about 10 Myr. Therefore, the surface density of CO starts to decline, but not as steeply as an exponential decline because the more CO is photodissociated the higher the surface density of carbon which indeed shields CO (negative feedback). By 10 Myr the carbon surface density and CO lifetime peak, after which CO declines steeply approaching a new and less massive quasi equilibrium (see blue dashed line in right panel). Carbon, on the other hand, decreases slowly with time due to accretion. This difference in the lifetime of CO vs carbon could be observed and tested, but at the moment there are not enough observations of carbon to constrain its lifetime.

If the starting mass is lower (bottom panel), CO is only slightly self-shielded given the lower CO mass input rate ($\dot{M}_{\text{CO}} \sim 0.2 M_\oplus \text{ Myr}^{-1}$). After 0.1 Myr, the carbon surface density is high enough at 100 au to shield CO and thus the surface density of CO increases until 3 Myr when it reaches its maximum. After a few Myr the CO mass input rate starts declining reducing both the CO and carbon surface densities (although the total carbon mass stays almost constant as the gas viscously spreads to larger radii).

An interesting consequence of the nature of how the mass input rate evolves is that at 100 Myr both scenarios have similar planetesimal disc masses ($\sim 10 M_\oplus$), and thus also fractional luminosities (f_{IR}) or dust masses. However, their gas content is not the same because it depends on the

mass loss rate integrated over time and thus there is some memory from their previous state. For example, if we compare the carbon final masses or surface densities, we find that in the high initial mass case they are a factor 10 and 3 larger, respectively. This is because the viscous evolution is slower than the collisional evolution as commented above.

Larger initial disc masses would increase this difference on the gas content even more, while keeping constant the disc mass at 100 Myr, thus unnoticeable from the amount of dust in the system (assuming gas and dust do not interact, see §5.6 for a discussion on this). On the other hand, much lower initial masses would result in an evolution with an almost constant \dot{M}_{CO} because it traces M^2 , where M is constant because the lifetime of the largest planetesimals is longer than 100 Myr, thus analogous to the picture presented in Figure 1a.

2.2.2 Low α

These differences in the final gas content are more extreme if the viscosity is lower, i.e. if the viscous evolution is slower, thus being even more sensitive to the evolutionary history of the system. As an example, in Figure 3 we show the evolution of two systems with the same initial masses as in Figure 2, but with a lower α value. For both examples, CO becomes shielded and stays as such beyond 100 Myr since the viscous timescale in this case is 60 Myr at r_{belt} , hence there is not enough time for the gas to viscously evolve and accrete onto the star. Therefore, at 100 Myr the differences in gas masses and surface densities are even larger between the two scenarios. For example, there is an order of magnitude difference in the final CO and carbon masses and CO surface density between the two scenarios. The carbon final surface density, on the other hand, is very similar for both scenarios, with differences only beyond 200 au.

Here we have found that not only the present mass input rate is important, but also the input rate in the past since this is likely to have started at a higher value. This adds a degree of extra complexity to the results shown in Kral et al. (2019, see their Figure 19), where it was shown that the carbon and CO mass depend on the viscosity and CO input rate (assumed to be constant). Moreover, the systems simulated here are far from a quasi steady state between 10–100 Myr, except for CO if the initial mass was low enough for CO to be unshielded in which case its evolution would follow the blue dashed line in Figures 2 and 3. But even in this case, the carbon surface density and mass will be out of equilibrium as the viscous evolution is slower than the fast decline rate of \dot{M}_{CO} . These degeneracies and non-linearity between the model parameters, initial conditions and subsequent evolution complicate the interpretation of observations of gas in debris discs, especially for shielded cases. Nevertheless, population studies can be used as a tool to constrain some of the model parameters by comparing observed and model distributions (see §3 below).

3 POPULATION STUDY FOR A STARS

In this section we study the gas component of a sample of A stars through population synthesis. This approach is ideal for degenerate problems such as the unknown initial disc

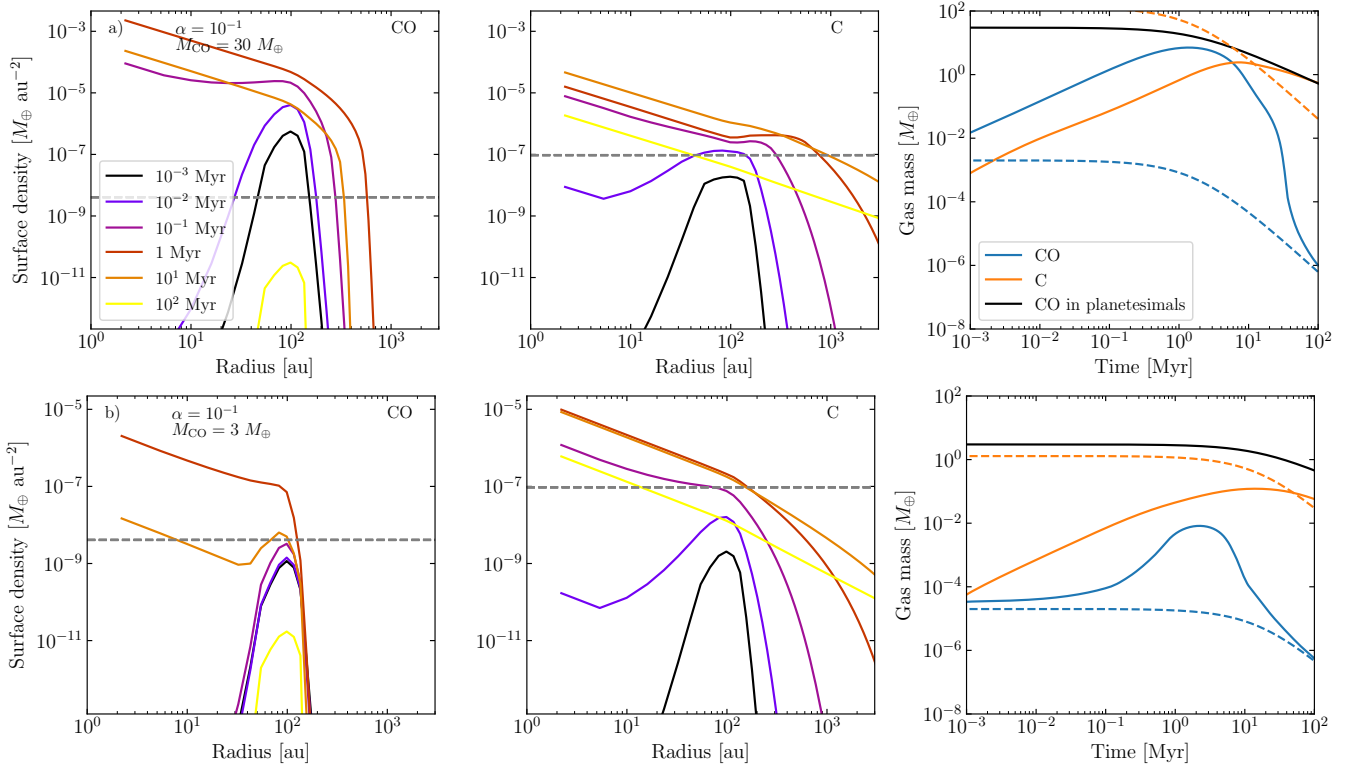


Figure 2. Same as Figure 1, but with a CO input rate decaying in time and high viscosity ($\alpha = 0.1$). **Top:** initial disc mass of $300 M_{\oplus}$ with a 10% CO fractional mass. **Bottom:** initial disc mass of $30 M_{\oplus}$ with a 10% CO fractional mass. In the right panels, the black line represents the CO mass that is still trapped in planetesimals and which decreases in time as the disc collisionally evolves. The steady state mass represented by dashed lines now decrease with time as the CO mass input rate declines.

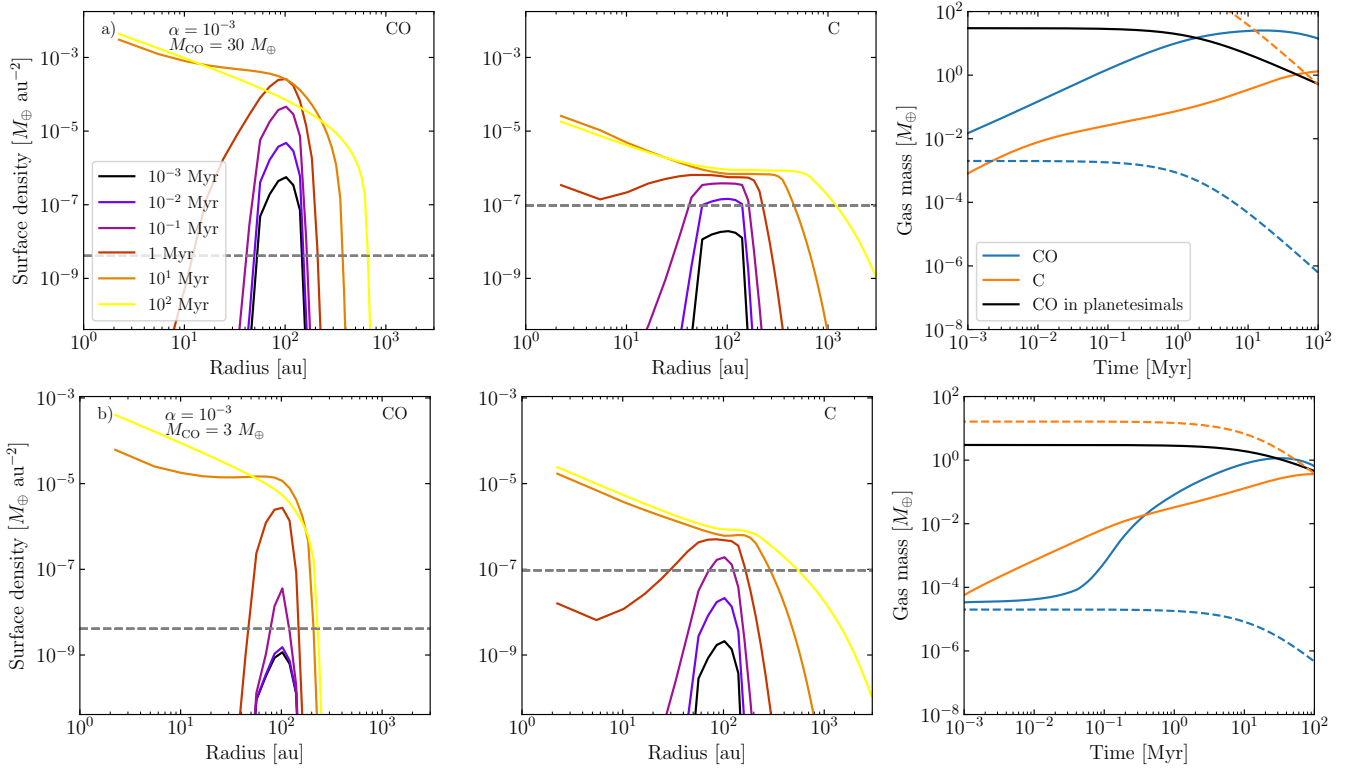


Figure 3. Same as Figure 2, but with a low viscosity ($\alpha = 10^{-3}$).

mass of a particular system, and can provide constraints on population properties. Our population synthesis model simulates the collisional evolution of their planetesimal discs and how the released gas would evolve in those systems. Here we use the results from Wyatt et al. (2007b) that used the same collisional evolution model to fit the observed distribution of disc temperatures and evolution of infrared excess (or f_{IR}) around A stars. Wyatt et al. used the distribution of observed 24 and 70 μm excess as a function of age to constrain the initial distribution of disc radii (approximating grains by blackbody spheres) and the maximum f_{IR} that a disc of a given age and radius can have. The latter is determined by planetesimal intrinsic properties and level of stirring. In particular, they assume all systems are born with a debris disc with a random blackbody radius between 3-120 au with a power-law distribution $N(r) \propto r^\gamma$ with $\gamma = -0.8$ and initial mass following a log-normal distribution with a mean of M_{mid} and a standard deviation of 1.14 dex. Because the initial fractional luminosity of discs is proportional to $M_{\text{mid}}D_{\text{c}}^{0.5}$ and the maximum fractional luminosity to $M_{\text{mid}}t_{\text{c}}D_{\text{c}}^{-0.5}$, Wyatt et al. (2007b) could constrain these products to $B \equiv M_{\text{mid}}D_{\text{c}}^{-0.5} = 1.3$ and $A \equiv D_{\text{c}}^{1/2}Q_{\text{D}}^{5/6}e^{-5/3} = 7.4 \times 10^4$, respectively, despite the degeneracy that exists between Q_{D}^* , e , I , D_{c} and M_{mid} .

To study the gas evolution, the main quantity we aim to obtain from previous dust studies is the mass loss rate since in our model it determines the gas input rate. However, the collisional evolution model used here does not fully constrain the total mass and mass loss rate of discs. This can be shown using Equations 10 and 11, and the products constrained by Wyatt et al. (2007b). We find that $\dot{M} \propto BM_{\text{mid}}/A$ for $t \ll t_{\text{c}}$ and AM_{mid}/B for $t \gg t_{\text{c}}$. This means that fixing A and B does not fully constrain \dot{M} , but further assumptions need to be made. Because the gas evolution is very sensitive to \dot{M} , one could try to vary D_{c} or M_{mid} to fit gas observations, but these parameters are degenerate with the fraction of CO in planetesimals. For example, increasing M_{mid} would increase the CO mass input rate generating larger gas masses, which could also be achieved by increasing the fraction of CO in planetesimals, or alternatively lowering the viscosity. Note that in principle, under certain assumptions one can estimate \dot{M} from the disc radius, emitting area (or fractional luminosity) and the mass of the particles that contribute the most to the disc's cross sectional area (e.g. Matrà et al. 2017b, Appendix B), without making assumptions about the large planetesimals in the disc. We discuss such an approach in §5.7. In this section we keep M_{mid} fixed to a default value and in §5.7 we show that our choice is roughly consistent with inferred mass loss rates from the dust emission.

Here we make two subtle changes to the relations that define A and B . First, we introduce a correction factor Γ which is the ratio between the true disc radius over the blackbody radius. This is necessary since the previous study used the *blackbody radius* (r_{BB}) when calculating collisional timescales (since it is the dust temperature which is fitted), which usually differs significantly from the true disc radius being on average underestimated (Booth et al. 2013; Pawellek et al. 2014; Pawellek & Krivov 2015). The difference is due to small grains that tend to have higher temperatures than blackbody spheres, therefore their distance to the star is usually underestimated when fitting blackbody

models to SEDs (note that the model in §2.2 is based on the true radius). Since the initial fractional luminosity is proportional to r_{belt}^{-2} , and the maximum fractional luminosity to r_{belt}^{-2} and t_{c} (with $t_{\text{c}} \propto r_{\text{belt}}^{13/3}$), with the introduction of Γ we obtain

$$D_{\text{c}}^{1/2} Q_{\text{D}}^{5/6} e^{-5/3} \Gamma^{7/3} = 7.4 \times 10^4, \quad (15)$$

$$M_{\text{mid}} D_{\text{c}}^{-1/2} \Gamma^{-2} = 1.3 \quad (16)$$

which is the same as used in Kains et al. (2011).

Second, the planetesimal strength can be parametrized as a function of planetesimal size, with $Q_{\text{D}}^* \propto D_{\text{c}}^{b_{\text{g}}}$ for planetesimal sizes above a few hundred meters (gravity dominated). For example, for compact planetesimals with sizes larger than a few hundred meters, simulations by Benz & Asphaug (1999) show $Q_{\text{D}}^* = 330D_{\text{c}}^{1.36}$. We will take this value as reference, although Q_{D}^* could be significantly lower if planetesimals are made of aggregates (see Krivov et al. 2018, and references therein). This change assumes however that the collisional evolution can still be approximated by $q = 11/6$ and Equation 10 where t_{c} is the lifetime of the largest body.

With these changes and a fixed value of Γ , the general evolution of fractional luminosities is left with only one degree of freedom, e.g. fixing e or M_{mid} leaves completely constrained the rest of the parameters. For $\Gamma = 1$ and assuming $e = 0.05$, we have the canonical values $D_{\text{c}} = 4.7$ km, $Q_{\text{D}}^* = 2700 \text{ J kg}^{-1}$, and $M_{\text{mid}} = 2.8 M_{\oplus}$, which are equivalent to the ones used in Wyatt et al. (2007b). For an arbitrary value of Γ and e we have for A stars

$$M_{\text{mid}} = 1.7 \left(\frac{e}{0.01} \right)^{0.5} \left(\frac{\Gamma}{1.7} \right)^{1.2} M_{\oplus}, \quad (17)$$

$$D_{\text{c}} = 0.2 \left(\frac{M_{\text{mid}}}{1.7} \right)^2 \left(\frac{\Gamma}{1.7} \right)^{-4} \text{ km}. \quad (18)$$

Here, we assume $\Gamma = 1.7$ which is in the middle of the observed range for A stars (1–2.5, Matrà et al. 2018b), and adopt the following values as standard: $D_{\text{c}} = 0.02$ km, $Q_{\text{D}}^* = 1.6 \text{ J kg}^{-1}$, and $M_{\text{mid}} = 0.5 M_{\oplus}$ and $e = 0.001$. Note that there are strong degeneracies between these parameters, and thus these cannot be interpreted physically. The values used here are chosen such that the mass loss rate in the discs that we model are roughly consistent with the mass loss rate inferred from their fractional luminosity (see §5.7).

We now proceed with these parameters and generate a random sample of 8,000 A stars. The mass of each star is randomly chosen between 1.7 and 3.4 M_{\odot} and its corresponding luminosity estimated using the mass-luminosity relation. The total disc mass is drawn from a log-normal distribution centred at M_{mid} and with a standard deviation of 1.14 dex as in Wyatt et al. (2007b). The planetesimal strength, mean eccentricity and maximum size are set to the values defined above, and we assume a CO mass fraction of 0.1. The disc radii are drawn following a power law distribution of exponent -0.8 and with a minimum and maximum radius of 5.1 to 204 au, consistent with Wyatt et al. (2007b) when Γ is set to a value of 1.7. Finally, we assume exocometary gas release starts at an age of 3 Myr (i.e. shortly after protoplanetary disc dispersal) and we evolve systems up to a random age between 3 and 100 Myr to get an age spread and we keep the value of α fixed to 0.1 (§3.1) or 0.001 (§3.2).

In the following sections 3.1 and 3.2, we compare the

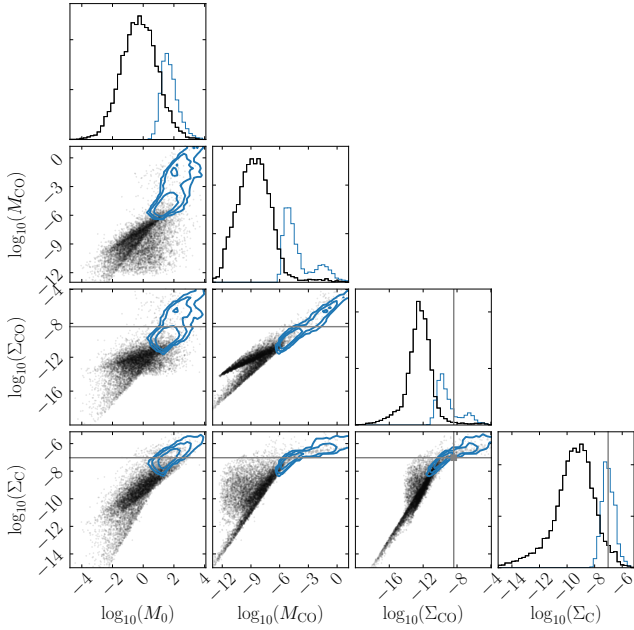


Figure 4. Distribution of the initial disc mass M_0 , final CO mass M_{CO} and final surface density of CO and carbon. The contours represent regions that enclose the 68%, 95% and 99.7% of the distribution of the filtered population. The grey lines represent the critical surface density over which CO and carbon can shield CO from UV photons. All variables are in units of M_{\oplus} or $M_{\oplus} \text{ au}^{-2}$. The marginalised distributions in the top panels are shown at an arbitrary scale for display purposes.

model distributions of CO and carbon masses to observations of a sample of A stars. To do so, it is important to first consider biases of any selected sample. We choose to compare our results with the complete sample of A stars within 150 pc that have been targeted by ALMA, and that meet the following criteria (Moór et al. 2017, the most complete study of gas around A stars with debris discs): i) disc fractional luminosity between 5×10^{-4} and 10^{-2} ; ii) dust temperature below 140 K; iii) detection at $\geq 70 \mu\text{m}$ with Spitzer or Herschel; and iv) age between 10 and 50 Myr. We apply the same filtering process to our synthesised sample to do a fair comparison between model and observations. In this way both observed and model samples have the same biases. In the following sections we present both whole and filtered model populations, representing them with small dots and blue contours, respectively².

3.1 High α

In Figure 4 we present the distribution of the initial disc mass (M_0), final CO mass contained within 500 au (at a random age between 3–100 Myr), and the final surface density of CO and carbon at the belt location, that result from our simulations. We overlay in blue contours the distribution of systems that would have been selected by Moór et al.

² To increase the number of points of this filtered sample we simulated 8,000 extra systems with the same initial random distribution, but that passed the Moór et al. selection criteria.

(2017). We find that the distributions of some parameters are highly correlated as expected. First, the more massive the initial disc mass is, the higher the amount of CO and carbon gas that will be present at a later epoch. For initial disc masses higher than $\sim 10 M_{\oplus}$, the CO mass distribution of the filtered sample extends to much higher values as CO becomes shielded. This is also true for the full population, but it is harder to see due to the age and radius spread which means that small warm discs with low initial masses can also reach shielded states for a short period. On the other hand, the surface density of carbon never reaches values as high as CO because the more carbon there is, the more CO is shielded and thus the lower carbon production rate.

The top panel of the second column shows the distribution of CO. While the bulk of the population is unshielded, the distribution has a tail extending to larger masses, with a small fraction (2%) having CO masses between $10^{-4} - 1 M_{\oplus}$ (the typical CO masses derived for shielded discs, Moór et al. 2017) or carbon surface densities at the belt location above the critical value to shield CO (4%). We find that applying the same selection mentioned above filters 99% of systems. Of the remaining 1%, 33% have CO masses higher than $10^{-4} M_{\oplus}$ displaying a bimodal distribution, and 49% have carbon surface densities above the critical value. These numbers are both consistent with the number of A stars that meet the selection criteria (17 of $\sim 8,000$ main sequence A stars within 150 pc) and with the statistics for shielded discs (i.e. 9/17 systems with CO masses $\gtrsim 10^{-4} - 1 M_{\oplus}$, Bovy 2017; Moór et al. 2017).

As expected, discs with large CO masses all have carbon surface densities above which shielding by carbon becomes important (grey lines). Note that there are no discs that are self-shielded but with carbon surface densities below the critical value. The reason for this can be understood by assuming quasi-steady state. Consider a disc with a constant input rate \dot{M}_{CO} . The minimum CO mass input rate such that CO is self-shielded is $\Sigma_{\text{CO,c}} \pi r_{\text{belt}}^2 / T_{\text{ph}}$ (assuming CO does not viscously spread and $\Delta r_{\text{belt}} / r_{\text{belt}} = 0.5$), while the minimum to reach carbon shielding is $7 \Sigma_{\text{C,c}} \pi \nu_0 r_{\text{belt}}$ (where $\nu = \nu_0 r$, Metzger et al. 2012). By equating these two expressions, we find that shielding by carbon will be more important in debris discs larger than

$$r_c = 7 T_{\text{ph}} \nu_0 \frac{\Sigma_{\text{C,c}}}{\Sigma_{\text{CO,c}}}, \quad (19)$$

which evaluated for $\alpha = 0.1$ gives 3 au (lower than the 5 au minimum disc radius considered here). Therefore, it is very unlikely to observe a disc in the bottom right corner of the intersection between the grey lines, i.e. only self-shielded. Lower viscosities will make r_c even lower. A caveat in this estimate is that for mass input rates much higher than the minimum to become shielded, at early times CO might become self-shielded before becoming shielded by carbon as shown in Figure 2.

In order to understand what is the dependence of the CO mass with the age, belt radius and fractional luminosity of a system, Figure 5 shows the scatter of these parameters for each simulated system and their distribution in blue when applying the selection criteria commented above. As a comparison, the red circles and triangles represent the CO detections and upper limits around A stars that meet the selection criteria (Moór et al. 2017; Kral et al. 2017; Kennedy

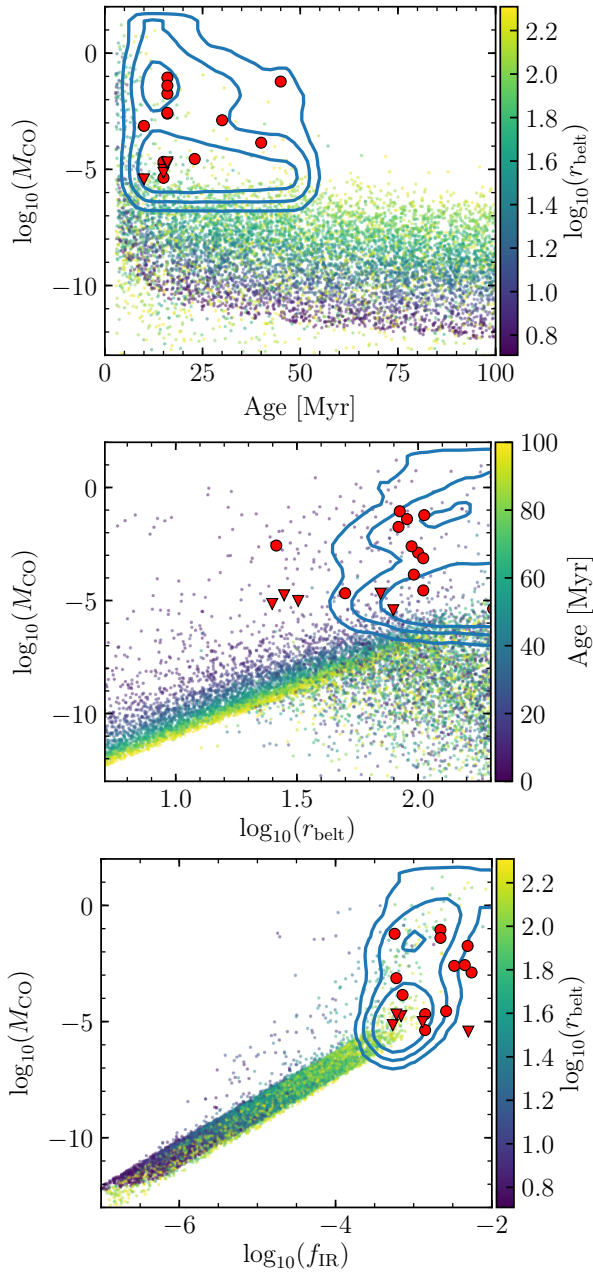


Figure 5. Population synthesis for A stars with $\alpha = 10^{-1}$. *Top:* CO gas mass (M_{CO}) in M_{\oplus} vs age. *Middle:* CO gas mass vs radius. *Bottom:* CO gas mass vs disc fractional luminosity. Each point corresponds to a different simulation. The contours represent regions that enclose the 68%, 95% and 99.7% of the distribution of the filtered population. The red circles and triangles represent the CO detections and upper limits around A stars that meet the same selection criteria as the filtered population.

et al. 2018; Booth et al. 2019; Hales et al. 2019, see Table A1). For the non-detections around HD 98363, HD 109832, HD 143675 and HD 145880 we use the non-LTE tool from Matrà et al. (2018a) to compute CO mass upper limits, assuming kinetic temperatures of 150 K and a radial distance of 1.7 their dust blackbody temperatures (their belts have not been resolved). The top panel shows M_{CO} vs age. This distribution reveals how the fraction of systems with large

CO gas masses decreases with time and by 50 Myr less than 1% of the whole population remain with CO masses higher than $10^{-5} M_{\oplus}$. The timescale at which shielded discs disappear is related to how fast gas viscously evolves, thus a smaller viscosity would result in long-lasting shielded discs as discussed in §2.2.2. Note that the distribution of red dots is consistent with the blue density map, and we do not expect CO masses lower than $10^{-7} M_{\oplus}$, which depending on line excitation conditions is at the limit of typical deep ALMA observations (e.g. Marino et al. 2016; Matrà et al. 2017b), but below the sensitivity of shallow CO surveys (e.g. Moór et al. 2017; Kral et al. 2017). Hence given the above selection cuts, the distribution of CO gas masses inferred from observations is consistent with our model. It is also worth mentioning that the CO mass estimates shown here have uncertainties that typically are an order of magnitude wide.

The middle panel of Figure 5 shows the distribution of M_{CO} vs r_{belt} . We find that the bimodal distribution of M_{CO} discussed above is present across the whole distribution of r_{belt} , and can be split into three populations, two with low CO masses and one with shielded and massive CO discs. For those systems that are unshielded, CO mass seems to increase with radius up to $r_{\text{belt}} \sim 50$ au after which the median CO mass decreases with radius. This is expected given that the CO mass in the unshielded case is simply proportional to the mass loss rate, which for $t \gg t_c$ is proportional to $t_c \propto r^{13/3}$ (Equation 14), whereas for $t \ll t_c$ is proportional to $1/t_c \propto r^{-13/3}$. The transition happens where $t_c \sim 50$ Myr (mean system age), which using M_{mid} we find this should happen at $r_{\text{belt}} \sim 56$ au. The larger dispersion for discs with a large radius is due to the mass input rate being proportional to M_0^2 (for $t \ll t_c$) which has a large dispersion. The third population is composed of shielded discs that exists predominantly in young systems with a high initial mass and with a large disc radius. We find that the distribution of observed discs matches reasonably well the expected distribution, with the exception of HD 121191, whose belt has not been resolved with enough sensitivity (we used 1.7 times its blackbody radius, which could be easily an underestimate, Moór et al. 2017), thus it could be significantly larger than the value used here.

The bottom panel of Figure 5 shows the distribution of M_{CO} vs fractional luminosity (f_{IR}). The fractional luminosity is calculated using Equations 14 and 15 in Wyatt (2008), but using the blackbody radius instead of the true radius. For $f_{\text{IR}} \lesssim 10^{-4}$ we find that M_{CO} is roughly proportional to f_{IR}^2 , a result that is expected since the CO release rate and mass loss rate in a belt is proportional to the square of the mass or f_{IR}^2 . On the other hand, for larger f_{IR} the CO masses grow steeply with fractional luminosity since CO is shielded in these systems. Overall, the observed distribution (red dots) is consistent with the filtered model population (blue contours) given the typical uncertainties in gas masses (~ 1 dex). The big exception is HR 4796. The CO mass upper limit for this system is below the blue 3σ confidence region by orders of magnitude. This disc has one of the highest fractional luminosities and is very narrow, hence the CO release rate should be high. Kennedy et al. (2018) concluded that the planetesimals must have a CO+CO₂ ice mass fraction below 2%. This is discussed further in §5.1.1.

Finally, in the top panel of Figure 6 we compare the carbon and CO masses of our models (contained within 500 au)

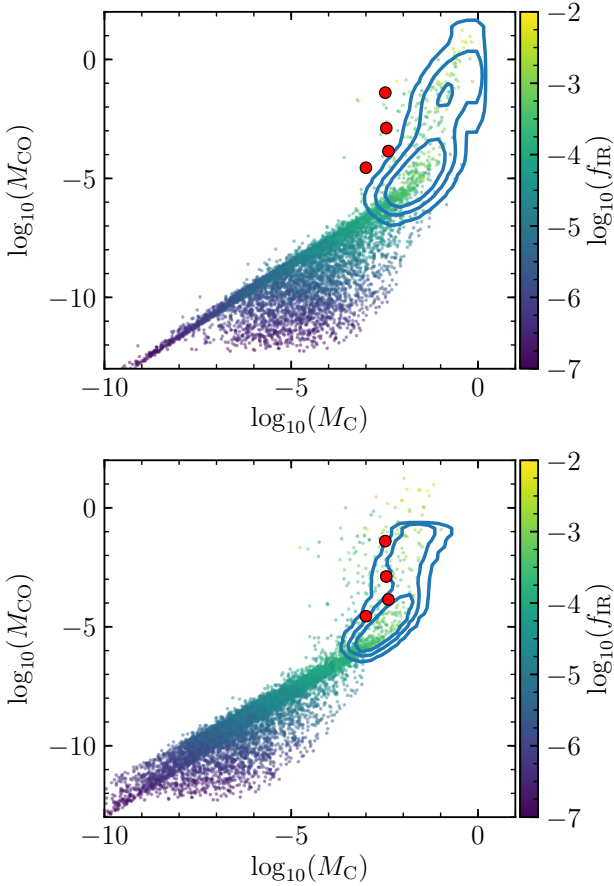


Figure 6. Population synthesis model for the carbon and CO masses around A stars assuming a high viscosity ($\alpha = 0.1$). **Top:** The carbon model mass represents all mass within 500 au. **Bottom:** The carbon model mass is calculated as $\Sigma_{C,r_{\text{belt}}}\pi r_{\text{belt}}^2$. Each point corresponds to a different simulation. The contours represent regions that enclose the 68%, 95% and 99.7% of the distribution of the filtered population. As a comparison, the red circles represent the CO and carbon detections around A stars that meet the same selection criteria as the filtered population.

with the estimated CO and neutral carbon mass in four discs (β Pic, 49 Ceti, HD 131835, HD32297, Higuchi et al. 2017, 2019; Cataldi et al. 2018; Kral et al. 2019; Cataldi et al. 2019). Overall we find that the observed carbon masses are lower than predicted by our model. This has been highlighted recently by Cataldi et al. (2018, 2019) and used to argue in favour of a scenario in which gas was released only recently in the β Pic and HD 32297 systems. This comparison is difficult since most of the carbon mass resides at large radii where typically ALMA observations are less sensitive (due to the primary beam and low surface densities). This is why we report gas masses as the total masses contained within 500 au, as a proxy for the *observable* mass. Note that this affects more the carbon mass than the CO mass, since carbon is always distributed up to larger radii. In steady state we expect the total carbon mass to be proportional to $r_{\text{max}}^{1/2}$ for $r_{\text{max}} > r_{\text{belt}}$ (Equation 9), so the observable mass could vary by a factor of a few if we used a different definition. This together with the low number statistics, unknown ionisation fraction (see 5.1.2) and uncertain excitation con-

ditions for the observed lines, hinders any strong conclusions on the model success at reproducing observations. If the carbon mass was indeed lower than predicted by our model, this could be due to a higher viscosity, however this would lower the CO mass of shielded discs in our model (lower shielding and shorter viscous timescale) making it inconsistent with observations. Alternatively we can estimate an observable carbon mass as the product between the carbon surface density at the belt location times the area of the belt, i.e. $\Sigma_{C,r_{\text{belt}}}\pi r_{\text{belt}}^2$ (for a fractional width of 0.5). This is shown in the bottom panel of Figure 6. Using this definition for carbon mass, we find a better agreement with observations. This illustrates that simple comparisons between model and observations are difficult. We identify the gas surface density at the belt location as a better quantity to test shielding models, since it is the vertical column densities of carbon and CO that set the CO photodissociation timescale in this context. Note that estimating the neutral carbon surface density from current observations is very difficult since the observed systems were edge-on (β Pic and HD32297) or marginally resolved (HD 131835). Moreover, the observed single carbon line in some of these systems is close to being optically thick and degenerate with excitation conditions, hindering determining the total carbon mass present (49 Ceti).

3.2 Low α

Using the same collisional evolution model as in the previous section, we use a lower $\alpha = 10^{-3}$ and make predictions for the mass of CO and carbon for a population of systems around A stars. Figure 7 shows the results for the CO mass as a function of age (top), r_{belt} (middle), and f_{IR} (bottom). We find a stronger bimodal distribution compared to the results with a high α . A larger fraction of systems become shielded and stay almost constant in time because the viscous evolution timescale for these discs is 100 times longer. Moreover, the CO masses of shielded discs are much higher because accretion is slower, and inconsistent with the observations (compare the blue contours with the red markers). In fact, even discs with low fractional luminosities which would have been undetectable with Spitzer or Herschel have high levels of shielded CO which hints at their high initial masses and fast collisional evolution. Because viscosity is low, CO gas takes much longer to disappear compared to solids. Therefore, the model in this paper disfavours low viscosities. Nevertheless, unbiased searches for CO have not been done around nearby A stars, thus we cannot rule out the presence of massive gas discs around stars without detectable debris discs.

Because the solid mass loss rate and thus the CO mass input rate are not fully constrained by the collisional evolution model used here, it might still be possible to fine tune parameters such that with a low viscosity the predicted CO masses are lower. We showed above that the mass input rate of the population is proportional to M_{mid} or $D_{\text{c}}^{0.5}$ (and constants), so in order to reduce the mass input rate by a factor of 100 to counteract the 100 times lower viscosity, we would need to reduce D_{c} by a factor of 10^4 , and thus also decrease M_{mid} by a factor 100 and increase Q_{D}^* by a factor 250. Such a large strength for such small bodies is unrealistic (Benz & Asphaug 1999), thus we conclude that α values as low as 10^{-3} are unlikely to explain the observed properties of gas in

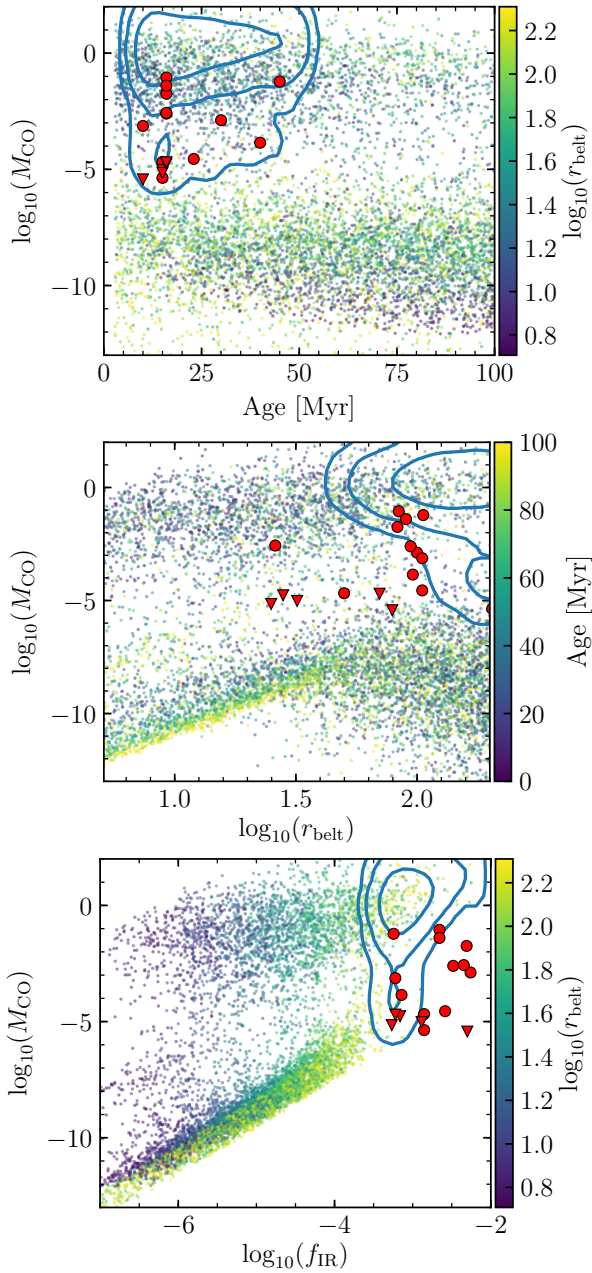


Figure 7. Population synthesis for A stars with $\alpha = 10^{-3}$. **Top:** CO gas mass (M_{CO}) in M_{\oplus} vs age. **Middle:** CO gas mass vs radius. **Bottom:** CO gas mass vs disc fractional luminosity. Each point corresponds to a different simulation. The contours represent regions that enclose the 68%, 95% and 99.7% of the distribution of the filtered population. The red circles and triangles represent the CO detections and upper limits around A stars that meet the same selection criteria as the filtered population.

high fractional luminosity discs. Moreover, high gas masses are only found in systems younger than 50 Myr (Greaves et al. 2016), thus favouring a viscous timescale shorter than 50 Myr at the belt location.

Another source of degeneracy is the assumed CO fraction in planetesimals. A lower CO abundance would lower the input rate of CO, which combined with a low viscosity could still fit the observed distribution of CO masses. This is

not explored in this paper, but in §5.2.1 we discuss avenues to break these degeneracies using independent observations.

4 SOLAR-TYPE STARS

Exocometary gas is not only found around A stars, but also around lower mass stars, from F to M (Marino et al. 2016, 2017; Lieman-Sifry et al. 2016; Matrà et al. 2019), however high CO mass discs are only found around A stars so far. This could be due to A stars being born with more massive discs on average, which was hinted by Matrà et al. (2019) based on a higher fractional luminosity in the more luminous stars that have been observed with ALMA. Here we aim to show that shielded discs are unlikely to be found around FGK stars simply because their planetesimal belts are born less massive than their A stars counterpart (or equivalently have a lower \dot{M}).

We take the same approach as for A stars, and we simulate a population of FGK stars following the results by Sibthorpe et al. (2018) that used both Spitzer and Herschel FIR photometry of 275 FGK stars to fit a collisional evolution model, similar to Wyatt et al. (2007b). That study found best-fit parameters $A = 5.5 \times 10^5$, $B = 0.1$ and $\gamma = -1.7$. We assume the same planetesimal strength relation as before, eccentricities of 0.001 and $\Gamma = 3.1$ (the average true to blackbody radius ratio for FGK stars resolved by ALMA, Matrà et al. 2018b). Fixing these parameters we have $D_c = 0.03$ km and $M_{\text{mid}} = 0.16 M_{\oplus}$ (vs 0.02 km and $0.5 M_{\oplus}$ for A stars), i.e. discs around FGK stars are born on average with a lower mass and lower fractional luminosities. We can anticipate that FGK stars will have lower mass CO discs, and for the same α value used here (0.1) viscosities will be slightly lower (a factor ~ 2) due to the different stellar masses and luminosities. We simulate then 8,000 FGK stars with stellar masses between 0.56 and $1.6 M_{\odot}$, blackbody radius between 1 and 1000 au (i.e. real radius between 3.1 to 3100 au) and ages between 3 and 100 Myr. Note that this large upper limit on the disc radius beyond 500 au is unrealistic given the observed population of debris and protoplanetary discs. Moreover, temperatures beyond 500 au might be below the CO sublimation temperature and thus CO would not be released. We keep this large upper limit because if not there is no guarantee that the model distribution would still fit the distribution of fractional luminosities of FGK stars. Nevertheless, because of the low value of γ only a very small fraction of simulated systems have radii larger than 500 au. Therefore, this unrealistic choice of upper boundary in the radius distribution does not affect our conclusions.

Similar to the previous figures, we present in Figure 8 the distribution of CO masses vs age, belt radius, and fractional luminosity. We find that overall the CO masses of the population are much lower, even after applying the same selection cuts as for A stars (blue contours, 2% of the whole population). This is because for a fixed fractional luminosity, the gas release rate is higher for more luminous stars (Matrà et al. 2019). We find that only 1% of the whole fraction has CO masses above $10^{-4} M_{\oplus}$, most of which are young systems with small discs. This fraction only grows to 4% for the filtered population. When we look instead at the carbon surface density at the belt location, we find that only 3% is

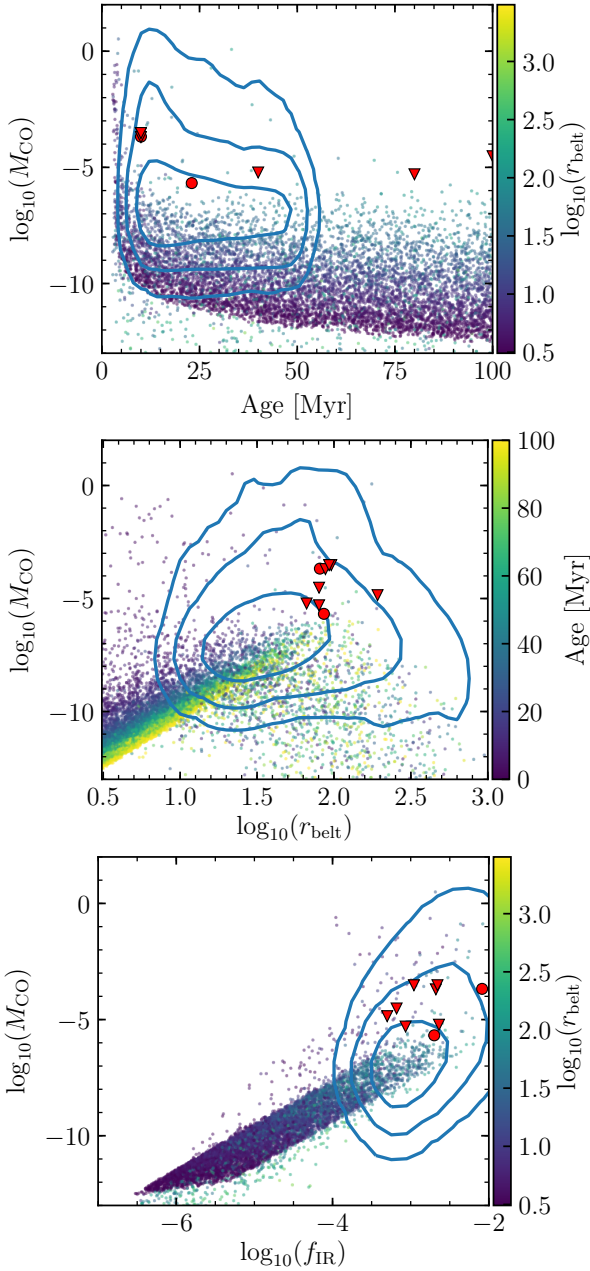


Figure 8. Population synthesis for FGK stars with $\alpha = 10^{-1}$. **Top:** CO gas mass (M_{CO}) in M_{\oplus} vs age. **Middle:** CO gas mass vs radius. **Bottom:** CO gas mass vs disc fractional luminosity. Each point corresponds to a different simulation. The contours represent regions that enclose the 68%, 95% and 99.7% of the distribution of the filtered population. The red circles and triangles represent the CO detections and upper limits around FGK stars that meet the same selection criteria as the filtered population.

above the critical value to shield CO, and this number increases only to 11% in the filtered population. Note that the filtered population is consistent with observations of FGK stars with bright debris discs represented by red circles and triangles (see Table A2). Our model then explains why we do not find hybrid/shielded discs around FGK stars as they are not as common given the collisional evolution models that fit their infrared excesses.

5 DISCUSSION

5.1 Caveats

In this section we discuss some of the assumptions made in our modelling, when these are justified and how replacing these by more complex models could have an impact on some of our conclusions.

5.1.1 Other volatiles

In this paper, we have focused on the release of CO only. Other volatiles that are abundant in Solar System comets such as H_2O , CO_2 , CH_4 , HCN , CN , C_2H_6 , NH_3 , H_2S , etc. could also be released in collisions that expose the interior of planetesimals. This will only happen if temperatures are high enough for thermal desorption (before or after collisions) or if there is a strong UV radiation so photodesorption is effective (Grigorieva et al. 2007). Assuming planetesimals at large radii are similar in composition to Solar System comets, we expect that only water and CO_2 to be as abundant or more than CO so their effect could be important in the model presented here. We expect that water thermal desorption will only be important interior to 10–20 au where blackbody temperatures are higher than 150 K around A stars, although photodesorption could act instead as the release mechanism at large radii. This could mean that the total amount of gas is higher by a factor of a few, but this would not affect the evolution of CO and carbon since the viscous evolution equations are scale independent for the mass and these molecules cannot act as shielding agents because they photodissociate at (UV) wavelengths longer than CO photodissociates and C ionises. The only noticeable effect on the gas would be that the oxygen to carbon ratio in the disc would be higher, which was used as an argument in Kral et al. (2016) to infer that water is also being released around β Pic, although not detected (Cavallius et al. 2019). On the other hand, including CO_2 would be equivalent to increasing the fraction of CO in planetesimals, since CO_2 is photodissociated into CO and oxygen in a timescale shorter than CO. Even if neutral carbon is present, it cannot shield CO_2 by more than a factor 0.33 (Rollins & Rawlings 2012), thus whether the CO in the model was released directly from collisions or is a result of CO_2 photodissociation has little effect. The only effect would be that the oxygen to carbon ratio in the disc would be higher, and even more if water is released too. A potential noticeable effect of including other volatile species could be that the higher gas density could increase the gas drag on the dust (see discussion in § 5.6).

One effect that could be important and neglected here, is that if temperatures of the largest planetesimals are higher than the water sublimation temperature, volatiles might not remain trapped in the interiors and planetesimals could devolatilise on short timescales compared to their collisional lifetime. Therefore, any conclusion on the evolution of gas in discs within 20 au must be taken with caution since gas released might not be controlled by collisional processes (e.g. Marino et al. 2017).

Moreover, in this paper we have assumed a constant CO abundance in planetesimals. This could not be the case since we expect that the CO abundances will depend both on the CO abundance in their progenitors protoplanetary discs, but

also on the disc temperature where planetesimals formed. If midplane temperatures at formation were close or higher than ~ 20 K (CO freeze out temperature), then planetesimals might lack CO. The best example for this possibility is HR 4796, which given that it is an A0 star and its belt is at only 79 au, it could well be that its planetesimals were formed within the CO snowline and thus poor in CO. In fact, HR 4796 is the system with the highest predicted midplane temperature at the belt location (see snowline locations in Figure 1 in [Matrà et al. 2018b](#)), or smallest radius compared to the CO snowline given its central star. Computing the effect of this temperature dependence on the CO abundance in planetesimals is difficult since it would involve knowledge of the temperatures in the parent protoplanetary disc. In addition, even if planetesimals were CO poor, they could contain large fractions of CO₂ which has a higher freeze out temperature. Therefore CO₂, which photodissociates very quickly and cannot be fully shielded by carbon, could be released producing large quantities of CO gas.

5.1.2 Carbon ionisation fraction

Here we discuss the effect of carbon ionisation on the results presented in this paper. This can be important since it is the carbon ionization continuum that can shield CO and explain the observed massive CO discs around A stars. In our model we neglect the presence of ionized carbon, or in other words we assume that the ionisation fraction of carbon is much lower than 1 (i.e. $\lesssim 0.3$). While carbon ionisation can be significant (e.g. in discs with low CO masses like β Pic C⁰/C ~ 0.015 – 0.2 , [Cataldi et al. 2014, 2018](#)), it has only been constrained by observations in one shielded disc (lower than 0.4 in HD 131835, [Kral et al. 2019](#)). Here we aim to show that the ionization fraction is lower than 0.3 for shielded discs, i.e. for discs with a carbon surface density higher than its critical surface density of $10^{-7} M_{\oplus} \text{ au}^{-2}$.

We calculate the ionisation fraction of carbon using Equation 15 in [Kral et al. \(2017\)](#), taking into account the stellar and interstellar radiation field ([Draine 1978](#); [van Dishoeck et al. 2006](#)) and assuming an optically thin medium (worst case scenario). In Figure 9 we present the ionisation fraction as a function of radius and carbon surface density for an A9V (top) and A0V star (bottom). The grey dashed horizontal line represents the critical surface density of neutral carbon for shielding and the continuous white contour represents a ionization fraction of 0.3. Overlaid in white dotted lines we plot the surface density expected for carbon in steady state ([Metzger et al. 2012](#)) if it is being input at 100 au at a rate of 10^{-1} and $10^{-3} M_{\oplus} \text{ Myr}^{-1}$ and with $\alpha = 0.1$. We find that the ionization fraction is always lower than 0.3 when densities are higher than the carbon critical density. Only within 3 au for the A0V star, the ionisation fraction is higher than 0.3 for surface densities above the critical value for shielding. Therefore we conclude that for our 1D model neglecting carbon ionisation is a valid assumption for shielded discs.

For low mass gaseous discs, the ionisation fraction can be close to one, specially for discs around early A type stars, although the ionisation fractions are likely lower when taking into account the optical depth in the UV. This high ionisation fraction has little effect on the lifetime of CO since it would be vertically unshielded even if all carbon were neu-

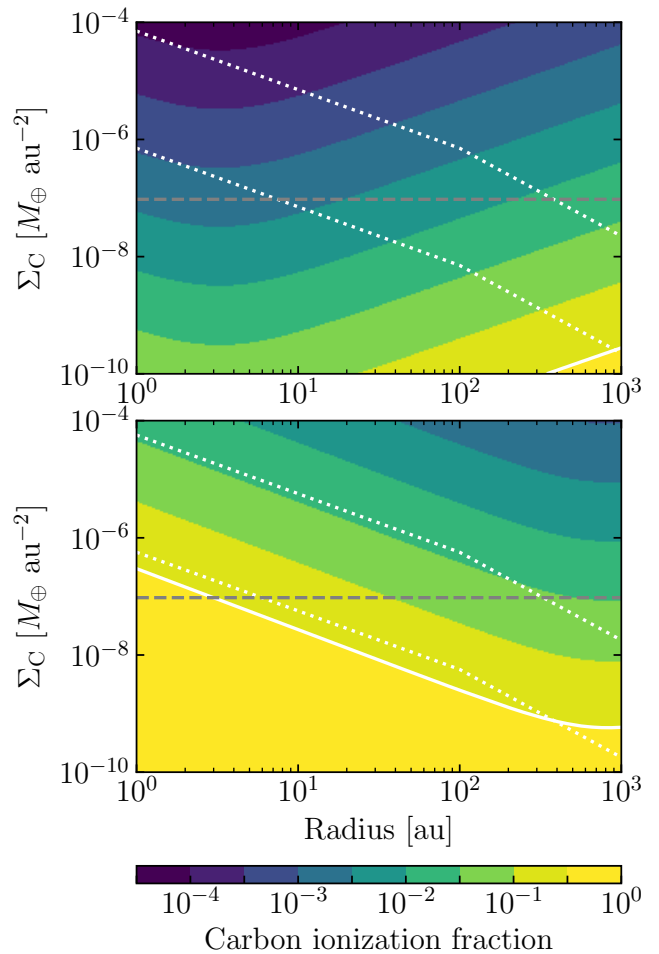


Figure 9. Carbon ionisation fraction as a function of radius and surface density around an A9V (top) and A0V star (bottom). The horizontal grey dashed line represents the critical density at which neutral carbon starts shielding CO. The white continuous line represents the 0.3 ionization level. The white dotted lines represent the expected surface density for a disc with a high viscosity ($\alpha = 0.1$) where carbon is being input at 100 au at a rate of 10^{-1} and $10^{-3} M_{\oplus} \text{ Myr}^{-1}$.

tral. Therefore, the evolution of these discs is not dependent on the level of ionisation. Note however that for those discs, the mass of neutral carbon that our model predicts could be overestimated.

A caveat in this calculation is that we are computing the ionisation fraction in the disc midplane, while the carbon atoms that could shield CO must lie in upper layers. Further work in 2D including the vertical dimension are necessary to estimate more precisely the ionisation fraction of carbon in the upper layers, as well as the vertically dependent UV radiation impinging the CO molecules (e.g. [Kral et al. 2019](#)). Moreover, here we only considered the photospheric emission, while these stars can have significant additional chromospheric emission in the UV ([Matrà et al. 2018a](#)). These considerations require of detailed modelling of the stellar emission and are beyond the scope of this paper.

5.1.3 CO photodissociation including stellar UV

Throughout this paper we have assumed that the photodissociation of CO is controlled purely by UV radiation impinging CO molecules in the vertical direction. This is only valid when the stellar UV flux is lower than the ISRF (e.g. for gas at 100 au around stars with luminosities below $\sim 20 L_\odot$) or if CO is shielded in the radial direction by carbon. We are interested in the second case since this could be common among massive discs independently of the stellar type. In order to check this we first compare the radial column density of neutral carbon in the radial (towards the star) and vertical direction (from the midplane), assuming the following: i) a disc surface density corresponding to an accretion disc with an input source at a belt radius of 100 au (Metzger et al. 2012); ii) a disc inner edge at R_\star ($2.1R_\odot$), 1 au and 50 au; iii) a surface density at 100 au equal to the carbon critical surface density ($10^{-7} M_\oplus \text{ au}^{-2}$); iv) a disc scale height of $0.05r$. Figure 10 shows these column densities as a function of radius. We find that the radial component is always orders of magnitude larger than the vertical one, even when using a disc inner edge of 50 au.

Then, in the case of a disc extending inwards until reaching the stellar surface, we calculate the CO photodissociation rate (Matrà et al. 2018a) around a A0 star considering shielding by carbon only. In the bottom panel of Figure 10, we compare the photodissociation timescale of four different cases or assumptions: ISRF only and no shielding; the ISRF plus the stellar radiation and no shielding; the ISRF only and vertical shielding (as in this paper); and the ISRF and stellar radiation and both vertical and radial shielding. We find that as expected, when neglecting carbon shielding (orange line), the photodissociation timescale is much lower than 120 yr. However, when considering carbon shielding (red and green lines) the photodissociation timescale is primarily set by the ISRF and vertical shielding. In fact, including the stellar contribution and the carbon shielding along the radial direction does not change significantly the CO photodissociation rate. We find this is true at 100 au even for low neutral carbon surface densities of $3 \times 10^{-12} M_\oplus \text{ au}^{-2}$, i.e. for all discs in the filtered model population and most of the discs that we model (see bottom right corner in Figure 4). Therefore we conclude that for the filtered population it is safe to neglect the stellar UV contribution to the CO photodissociation.

5.2 Breaking degeneracies

5.2.1 Measuring α

As commented in §3.2, in our population synthesis model a degeneracy exists between the kinematic viscosity (or α) and the fraction of CO in planetesimals. A potential way to break this is by estimating the level of turbulence in the disc through line observations and thus constraining α independently. Generally speaking, the local line width of an emission line in velocity units (without taking into account Doppler shifts due to Keplerian rotation) is

$$\Delta v_{\text{line}} = \sqrt{2k_B T / (\mu m_p) + v_{\text{turb}}^2}, \quad (20)$$

where T is the gas temperature, μ the mean molecular weight, m_p the proton mass, and v_{turb} is the turbulent

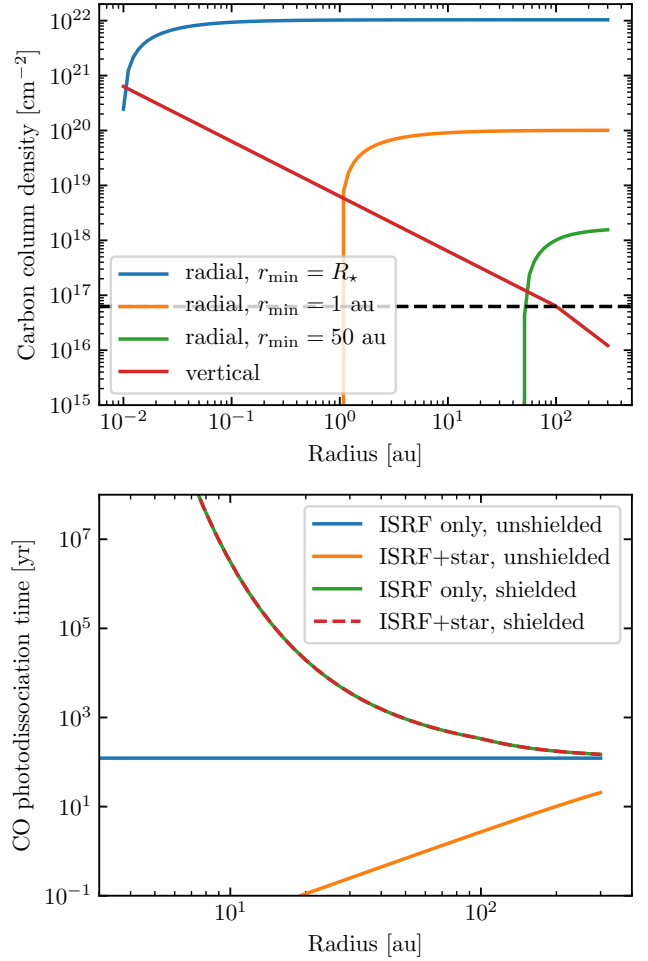


Figure 10. *Top:* Column density of carbon in the radial (towards the star) and vertical (from the midplane, red line) directions. The radial component is shown for three different cases in which the disc inner edge is at the stellar surface ($2.1R_\odot$), 1 au and 50 au (blue, orange and green lines). The horizontal dashed black line represents the critical column density of carbon above which it can effectively shield the CO. *Bottom:* CO photodissociation timescale assuming a carbon disc extending down to the stellar surface and calculated in four different scenarios: radiation dominated by the ISRF and neglecting shielding (blue), radiation dominated by the ISRF and considering shielding (green), radiation from the ISRF and an A0 star and neglecting shielding (orange line), and radiation from the ISRF and an A0 star and considering shielding (red dashed line).

linewidth³. The turbulent line width can be approximated by $\sqrt{\alpha} c_s$, thus obtaining $\Delta v_{\text{line}} = c_s \sqrt{2 + \alpha}$, where c_s is the sound speed. Therefore, if we can constrain c_s from the disc scale height or temperature (e.g. through line excitation temperature, line brightness from optically thick emission or dust observations), then α could be constrained independently from our population synthesis model, allowing to constrain the fraction of CO in planetesimals. This idea is not new, and multiple studies exist in protoplanetary discs

³ Note that Δv_{line} is defined as $\sigma_{\text{line}} / \sqrt{2}$, with σ_{line} being the standard deviation of the line profile

trying to constrain α through line observations (e.g. Hughes et al. 2011). The difference here is that a larger α value compared to protoplanetary discs should be easier to observe and the vertical dependence of the temperature should be weaker since these discs are optically thin.

In order to constrain α to values near 0.1, it would be necessary to constrain the line FWHM with a precision below 1%, which is achievable with high S/N observations that can resolve the line intrinsic widths. The precision or fractional uncertainty on the line FWHM can be written as (Lenz & Ayres 1992)

$$\frac{\sigma_{\text{FWHM}}}{\text{FWHM}} = 1.4 \sqrt{\frac{\Delta\nu}{\text{FWHM} (S/N)_0}}, \quad (21)$$

where $\Delta\nu$ is the spectral resolution and $(S/N)_0$ is the S/N at the line peak. Since the peak S/N typically scales as the square root of the spectral resolution for well resolved lines, it can be shown that the expression above is equivalent to

$$\frac{\sigma_{\text{FHM}}}{\text{FWHM}} = \frac{0.24}{(S/N)}, \quad (22)$$

where S/N is the integrated line signal-to-noise. This form shows that as long as the line is well resolved, the precision to measure the linewidth does not depend on the spectral resolution, but only on the integrated line S/N (which does not depend on $\Delta\nu$ for ALMA observations). The above expression then implies that in order to constrain the linewidth with a precision of 0.2%, it is necessary to achieve an integrated line S/N greater than 100. Although such high S/N might be difficult to achieve over a single beam, azimuthal averaging with Keplerian masking can be employed (e.g. Matr a et al. 2017b; Teague et al. 2018) and thus obtaining high precision measurements of the intrinsic linewidth and constraints on α .

5.2.2 Measuring the CO fraction in planetesimals

The degeneracies between α and fraction of CO in planetesimals (f_{CO}) could also be broken by estimating f_{CO} in unshielded discs. Because the CO mass in those discs only depends on the photodissociation timescale (t_{ph}) and the product between the mass loss rate and f_{CO} , i.e. $\dot{M}_{\text{CO}} = t_{\text{ph}} f_{\text{CO}} \dot{M}_{\text{CO}}$, by estimating the UV field at the CO location and mass loss rate from the disc fractional luminosity it is possible to derive f_{CO} as shown by Marino et al. (2016) and Matr a et al. (2017b). The main obstacle for determining f_{CO} with this method are the uncertainties on the CO masses due to NLTE effects. Observations of multiple transitions could help improve these mass estimates (Matr a et al. 2017a).

5.3 Resolved observations of atomic carbon

An important test of the model presented here and previous viscous evolution modelling is to check whether the atomic gas is more spread than CO and planetesimal belts, with a surface density characteristic of an accretion disc and thus decreasing with radius. So far, the four resolved observations of atomic carbon have not found that, but rather inner cavities in the neutral carbon distribution (Kral et al. 2019; Cataldi et al. 2018, 2019; Higuchi et al. 2019). This could be due to low viscosities, but that would contradict our findings that high viscosities are preferred. Alternatively, it could be

that carbon is significantly ionised within a few tens of au, although even the ionised carbon in β Pic was found to have a large inner cavity (Cataldi et al. 2014). Thus, it might be that something is preventing carbon from spreading inwards. As commented before, around A stars carbon can become unbound due to radiation pressure, but we expect both self-shielding and collisions with bound oxygen atoms to prevent this. If radiation pressure was stronger than previously estimated though (e.g. Kral et al. 2017), this could explain the gas cavities observed so far. In fact, there is already evidence that the stellar UV flux where most of the stellar absorption occurs could be underestimated around these young A stars (e.g. Deleuil et al. 2001; Bouret et al. 2002). Matr a et al. (2018a) compared observed and photospheric model UV spectra for β Pic finding it was underestimated by orders of magnitude. If both carbon and oxygen are loosely bound, then this could explain why carbon is not forming an accretion disc.

A counter argument for this possibility is that if carbon and oxygen were not spreading inwards due to radiation pressure and instead accumulating near the planetesimal belt, then the carbon surface densities should be even higher, which is inconsistent with the observed carbon masses and analysis presented here. Only if radiation pressure can remove carbon from the system or at least beyond the planetesimal belt this could solve this apparent inconsistency. Alternatively, the gas distribution could still have large cavities if the gas was released recently in a giant collision, as suggested by Dent et al. (2014) and Cataldi et al. (2018, 2019), or the disc was stirred only recently (in less than a viscous timescale) and thus gas release has only been in place for a small fraction of the ages of these systems. This however raises even more questions regarding the frequency of these events since we would also expect to observe systems where gas has viscously spread filling the cavities with gas.

5.4 Interaction with planets

The gas evolution modelled here does not take into account any possible interaction with planets. These planets might be massive and thus significantly affect the gas distribution and evolution, or small enough such that any exocometary accreted gas could dramatically change the mass and composition of their atmospheres. Because the accretion of gas onto low mass planets requires detailed modelling, we leave this topic for future work. Here we focus on the effects that massive planets could have on the gas distribution, which can be studied using simple relations. For a more detailed discussion on planet disc interactions see Kral et al. submitted.

Similarly to the study of planet disc interactions in protoplanetary discs, there is a critical planet mass above which a planet could create a deep gap in the gas distribution around its orbit and affect the gas transport processes in the system (e.g. Crida et al. 2006). Such a planet can reduce the gas flow from the planetesimal belt (exterior to the planet's orbit) into the inner regions of the system, creating a cavity (Lubow et al. 1999; Lubow & D'Angelo 2006). This scenario is of particular interest here as it could solve the tension between the few carbon observations that show cavities and the viscous evolution models of exocometary gas in the literature (as suggested by Cataldi et al. 2019). Thus,

the question is how massive must a planet be to reduce the gas flow. Both analytic and numerical studies have shown that the accretion rate onto the star can be a factor 4–10 times lower than the accretion rate outside of the orbit of the planet for planet-to-star mass ratios of $5 \times 10^{-5} - 10^{-3}$ (Lubow & D’Angelo 2006). In this case, most of the gas flowing through the planet’s orbit will be accreted by the planet. One of the basic requirements to create such gaps and affect the radial flow is that the Planet’s Hill radius must be larger than the disc scale height. Defining the vertical aspect ratio of the gas disc as $h = H/r$, where H is the scale height of the gaseous disc, we find that in order to explain the observed cavities planets must be more massive than

$$M_p > 50 \left(\frac{h}{0.03} \right)^3 \left(\frac{M_\star}{2 M_\odot} \right) M_\oplus. \quad (23)$$

This minimum planet mass is thus very sensitive to the disc scale height. Assuming blackbody temperatures for the gas and a mean molecular weight of 14 (i.e. gas is dominated by carbon and oxygen) we find $h \approx 0.03$ at 40 au. Gas temperatures could be much lower (as suggested by the low excitation temperature of CO in some discs, Kóspál et al. 2013; Flaherty et al. 2016; Matrà et al. 2017a) and the mean molecular weight larger if dominated by CO, which would make h and the minimum planet mass smaller. So far, 49 Ceti is the only example there is where h has been constrained for the gas. Hughes et al. (2017) constrained h to be smaller than 0.04⁴ and therefore planets with masses similar or larger than Neptune could explain the observed carbon cavities. Note that planets with masses below a few Jupiter masses are currently undetectable through direct methods (e.g. direct imaging, Bowler & Nielsen 2018), thus the non-detections of planets within these cavities are still consistent with this scenario. Moreover, we can hypothesise that the inner edges of the observed planetesimal discs are truncated by planets, similar to the Kuiper belt in the Solar System. These planets could also be the ones responsible for stirring the orbits of planetesimals igniting a collisional cascade and the gas release (e.g. Mustill & Wyatt 2009). Therefore the radial distribution of gas could provide important constraints to the presence of planets that are undetectable with current instrumentation.

These massive planets decreasing the inward flow of gas would accrete most of it (e.g. Machida et al. 2010). We can calculate the planet accretion rate using Equation 3 and the analytic solution for the surface density of gas by Metzger et al. (2012) for an α disc model. In steady state and assuming only a small fraction of the gas flow is able to cross the gap, we find $\dot{M}_p = 3\pi\nu\Sigma$, which for a given disc is independent of radius as long as the planet is interior to the planetesimal belt where gas is being released. Evaluating this expression we find

$$\dot{M}_p = 10^{-2} \left(\frac{\alpha}{0.1} \right) \left(\frac{\Sigma_G(r_{\text{belt}})}{10^{-7} M_\oplus \text{ au}^{-2}} \right) \left(\frac{r_{\text{belt}}}{100 \text{ au}} \right) \left(\frac{\mu}{14} \right)^{-1} \left(\frac{M_\star}{2 M_\odot} \right)^{-1/2} \left(\frac{L_\star}{16 L_\odot} \right)^{1/4} M_\oplus \text{ Myr}^{-1}. \quad (24)$$

Therefore, over 10–100 Myr of evolution we do not expect that the gas accretion will significantly change the mass of

such a planet. Nevertheless, because the gas will be dominated by carbon and oxygen (in contrast to protoplanetary disc gas dominated by H₂) the abundance of these elements relative to hydrogen could change significantly. Even the abundance of carbon relative to oxygen (the C/O ratio) could be affected since the accreted gas could have a low C/O if originating from CO₂ or H₂O outgassed molecules compared to gas accreted during the protoplanetary disc phase with a C/O ratio close to one at tens of au (e.g. Öberg et al. 2011). Finally, the accretion luminosity of such an accreting planet will be $\sim 10^{-9} L_\odot$, assuming a planet mass of 50 M_\oplus and a radius of 6 Earth radii. Therefore it is unlikely that exocometary gas accretion will increase the intrinsic luminosity of these young planets (Mordasini et al. 2009).

5.5 Other gas removal processes

If gas were not being removed through viscous accretion onto the star or planets, then some other mechanism must be at play. We identify two potential candidates: radiation pressure acting on the gas and unbound grains pushing the gas out (Tazaki & Nomura 2015; Kuiper & Hosokawa 2018). For example, radiation pressure could remove mass in the form of winds launched from the surface of the disc where densities are low enough that atomic carbon is unshielded from stellar radiation. We have already discussed in §5.3 that radiation pressure on carbon could be underestimated by current models (e.g. Kral et al. 2017) and thus this scenario cannot be ruled out yet. If so, the α value derived here gives a sense for the timescales involved. We found that observations were best matched with $\alpha = 0.1$, which leads to a viscous timescale of 0.6 Myr or ~ 700 orbits for gas released at 100 au around a 2 M_\odot star. This means that the mechanism is not efficient enough to remove the bulk of the gas mass on a dynamical timescale, which is expected given the large optical depth in the radial direction at the frequencies where gas absorbs and low dust densities. Detailed modelling of these processes with more accurate stellar spectra are required to test these mechanisms.

5.6 Gas - dust interactions

So far through this paper we have neglected how gas could affect the dynamics of dust; particularly, how gas could damp the eccentricity of small dust grains in high eccentricity orbits or unbound trajectories due to radiation pressure, and how gas could drag small dust interior or exterior to the planetesimal belt on timescales shorter than collisions or P-R drag. Here we aim to quantitatively check if gas could affect the dust dynamics in the context of shielded discs (see also Kral et al. 2019).

First, to understand whether gas drag could be important we compute the dimensionless stopping time (or Stokes number)⁵ of grains of different sizes and at different radii around an A3V star (Figure 11 top panel). We assume a steady state surface density of gas (Metzger et al. 2012) for a system where gas is released from a planetesimal belt at 100 au and the surface density of gas at 100 au is $10^{-6} M_\oplus \text{ au}^{-2}$ —a typical surface density for the predicted

⁴ calculated at 40 au using their best fit parameters

⁵ Using the subsonic stopping time.

distribution of shielded discs (see Figure 4). We find that all grains above the blowout size (dashed horizontal line) have Stokes numbers larger than 10 near 100 au where dust is released (in between the vertical dashed lines), and thus we do not expect grains to be significantly damped before experiencing disrupting collisions. In particular, mm-sized grains have Stokes numbers of $\sim 10^4$, thus are well decoupled from the gas. Nevertheless, we find that sub- μm grains below the blowout size have Stokes number close and below unity, and thus these unbound grains could remain in the system for longer timescales due to gas drag. The dynamics of such grains has been studied by [Lecavelier Des Etangs et al. \(1998\)](#), finding that unbound dust grains can be heavily decelerated by gas drag creating a stationary outflow. Therefore, gas rich debris discs might have more massive halos of small grains which can be traced in scattered light (e.g. HD32297, [Schneider et al. 2005](#); [Bhowmik et al. 2019](#)).

Even though grains above the blowout size have larger Stokes numbers, they could still systematically migrate in or out due to a difference in their orbital speed. Ignoring Poynting-Robertson drag (PR drag), the azimuthal velocity of a dust grain on a circular orbit is

$$v_\phi = v_K(1 - \beta)^{1/2}, \quad (25)$$

where β is the ratio between the radiation and gravitational forces ([Burns et al. 1979](#)), thus small grains in circular orbits will have sub-Keplerian speeds. Similarly, because of pressure support gas will also orbit at a sub-Keplerian speed that is

$$v_g = v_K(1 - \eta)^{1/2}, \quad (26)$$

$$\eta = -\frac{1}{r\Omega_K^2\rho_g} \frac{dP_g}{dr}, \quad (27)$$

where ρ_g and P_g are the gas density and pressure, respectively, and η the ratio between the pressure gradient force and gravitational force. If $\beta > \eta$, dust grains will orbit slower than the gas, and thus gas drag will increase their angular momentum producing an outward migration ([Takeuchi & Artymowicz 2001](#)). In the middle plot of Figure 11 we show the ratio β/η for different grain sizes at different radii. We calculate β assuming blackbody grains with an internal density of 2.7 g cm^{-3} and η according to blackbody temperatures and the analytic expression for the gas surface density profile. We find that grains below 1 mm have $\beta > \eta$ and thus will experience outward migration, while larger grains will tend to migrate inwards. This will only happen if the timescales are shorter or comparable to the collisional lifetime of these grains. Using Equation 26 in [Takeuchi & Artymowicz \(2001\)](#), which assumes circular orbits, we compute the radial velocity of grains under the influence of gas and PR drag too (Figure 11 bottom panel). We find that for small μm -sized grains their radial speed could be a few percent of the Keplerian speed, and thus could exit the planetesimal belt within a few orbits.

Small grains will only migrate out of the belt efficiently if they can do so on a timescale shorter than their collisional timescale. In Figure 12 we compare the timescale at which a small grain at the bottom of the collisional cascade on a circular orbit would exit the belt, assuming a disc width of 50 au, with their collisional timescale as a function of the disc fractional luminosity. For this, we use equations B5 and B6

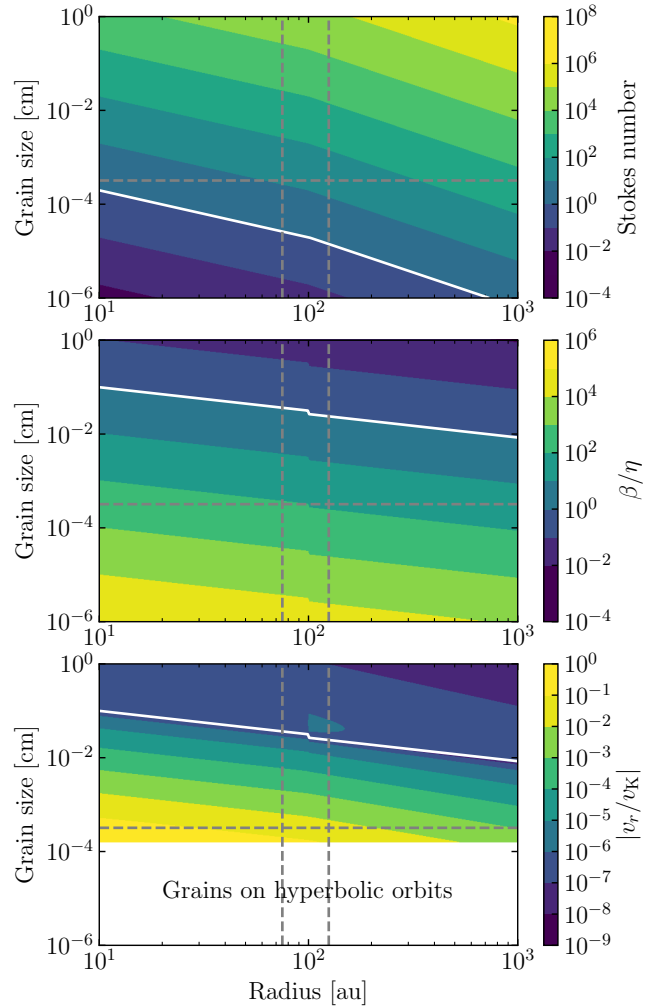


Figure 11. Effect of gas on dust as a function of grain size and stellar distance assuming a steady state surface density of gas when released at 100 au, reaching a local surface density of $10^{-6} M_\oplus \text{ au}^{-2}$. **Top:** Dimensionless stopping time of Stokes number in the subsonic regime. The white line represents a Stokes number of one. **Middle:** Ratio between the β (the radiation to gravitational force ratio) and η the ratio between the pressure gradient force and gravitational force. If larger than 1, then grains will be pushed outwards and vice versa. **Bottom:** Modulus of the radial velocity of dust grains over the Keplerian velocity. In the three panels, the horizontal dashed line represents the blowout size for a A3V star and the vertical dashed lines represent the inner and outer edge of a belt at 100 au with a fractional width of 0.5.

in [Matrà et al. \(2017b\)](#) to calculate the mass loss rate and collisional timescales. We also assume a CO mass fraction of 0.1 inside planetesimals, which sets the gas release rate and thus the gas surface density which will affect the dust. We find that for $\alpha = 0.1$ (blue line) and fractional luminosities larger than 10^{-3} , grains can exit the belt on timescales shorter than their collisional lifetime (blue line is below the dashed black line). For smaller f_{IR} drift timescales due to gas drag become too long, and actually, for $f_{\text{IR}} < 6 \times 10^{-5}$ PR drag dominates as a drag force (see the blue line converging to the black dotted line). Nevertheless, PR drag timescales

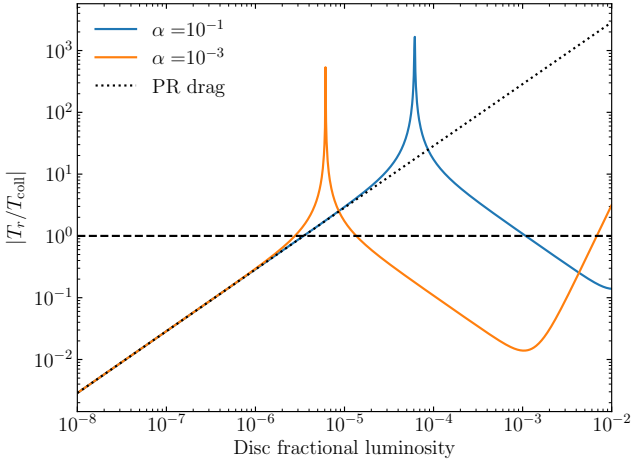


Figure 12. Radial migration timescale over collisional timescales for dust grains at the bottom of the collisional cascade. The blue and orange lines represent a case with an α viscosity value of 10^{-3} and 0.1 , respectively. The black dotted line represents a case when neglecting gas drag and considering PR drag only.

will be longer than collisional timescales for $f_{\text{IR}} > 4 \times 10^{-6}$, which is at the limit of detectability with current instrumentation (see Wyatt 2005, for a detailed discussion on PR drag). For smaller α 's, gas drag could become important even in less massive planetesimal discs since gas can accumulate for longer and thus build larger gas surface densities. For $\alpha = 10^{-3}$, small dust in discs with $f_{\text{IR}} > 2 \times 10^{-5}$ could efficiently migrate outwards with the fastest drift achieved with $f_{\text{IR}} \sim 10^{-3}$, which is when the Stokes number for grains with $\beta = 0.5$ is equal to 1. Therefore, we conclude that outward migration of small dust grains due to gas drag in exocometary gaseous discs could be an efficient process, increasing the cross sectional area of disc halos (e.g. HD32297, Schneider et al. 2005; Bhowmik et al. 2019).

Based on the derived Stokes numbers we find that photoelectric instability (Lyra & Kuchner 2013; Richert et al. 2018) should not play a major role affecting the distribution of gas and dust. This is because the Stokes numbers are significantly larger than unity for all grains sizes above the blowout size, and the dust-to-gas ratio is expected to be much lower than unity when considering only grains smaller than $10 \mu\text{m}$ as in Richert et al. (2018, see their Figure 2).

Finally, it is possible that the overall gas surface densities are higher than assumed here if other volatiles (e.g. water) are being released as well. Assuming a water ice fraction of 0.5 in planetesimals, the gas surface densities would be a factor 5 larger than assumed. Therefore, dust grains close to the blow-out size would have lower Stokes numbers in the range $1-10$ (as suggested in Bhowmik et al. 2019), and migrate outwards even faster. Note that the smaller Stokes number could be enough to trigger the photoelectric instability, although the higher gas surface density would also decrease the dust-to-gas ratio. Detailed simulations are necessary to assess whether this instability could act on timescales shorter than the age of these systems with these dust-to-gas ratios and Stokes numbers.

5.7 Mass loss rate inferred from the SED

In this paper we have shown that overall CO gas observations around A stars can be explained with our population synthesis model presented in §3. Nevertheless, this is not entirely satisfactory since our model has three main free parameters to fit one main observable, the observed CO gas mass. Moreover, these parameters (the viscosity, the fraction of CO in planetesimals, and the maximum planetesimal size or initial median disc mass) are degenerate. In §5.2.1 and §5.2.2 we discuss how the first two could be constrained through independent methods and thus break degeneracies. The maximum planetesimal size is however unconstrained by the collisional model used here. Namely, given a disc radius and fractional luminosity, the total disc mass and mass loss rate are unconstrained. Matrà et al. (2017b) showed however that the mass loss rate at the bottom of the collisional cascade can indeed be estimated analytically based on the disc cross sectional area and minimum grain size. The reason for this is that the lifetime or collisional rate of the smallest grains (near the blowout size) is dominated by grains of similar size which is not the case at the top of the size distribution. This slight but significant difference is not accounted for in the collisional model used here which assumes a single power law size distribution.

In Figure 13 we compare the mass loss rate used in our model (§3) vs the mass loss rate that would be inferred from the model fractional luminosity using Equation B6 in Matrà et al. (2017b). We find that for the chosen parameters ($e = 0.001$, $D_c = 0.02 \text{ km}$, $Q_D^* = 1.6 \text{ J kg}^{-1}$ and $M_{\text{mid}} = 0.5 M_{\oplus}$) the mass loss rate in our model roughly agrees with the one calculated considering the bottom of the collisional cascade ($\dot{M}_{D_{\text{min}}}$), except for belts with radius smaller than $\sim 50 \text{ au}$. The dependence on belt radius is due to both analytic expressions having a different dependence on r_{belt} . The belt radius sets the Keplerian and relative velocities, which are important for determining the minimum planetesimal size that disrupt the planetesimals at the top of the size distribution, whereas at the bottom of the size distribution that size is simply set by the blowout size. In order to reconcile the mass loss rate from small grains and the largest planetesimals, more detailed modelling is necessary taking into account, for example, the size dependent planetesimal strength and wavy patterns in the size distribution (Krivov et al. 2006; Thébaud & Augereau 2007).

5.8 Hydrodynamic limit

Finally, here we discuss whether it is reasonable to treat the evolution of exocometary gaseous discs with the standard viscous evolution equations used here. While these equations are normally valid for the evolution of protoplanetary discs, the gas densities in the exocometary gas context can be much lower and thus we may approach the limit at which these equations are valid. To check this, we compare the disc scale height ($H = c_s/\Omega_K$) with the mean free path in the gas, l (see Kral et al. 2016, for a specific discussion related to $\beta \text{ Pic}$'s gaseous disc). We find that at 100 au , the mean free path of gas (not ionised) in the midplane will be smaller than H as long as the gas surface density is larger than $\sim 10^{-9} M_{\oplus} \text{ au}^{-2}$. If the gas is highly ionised as expected for low density discs, the mean free path will be orders of

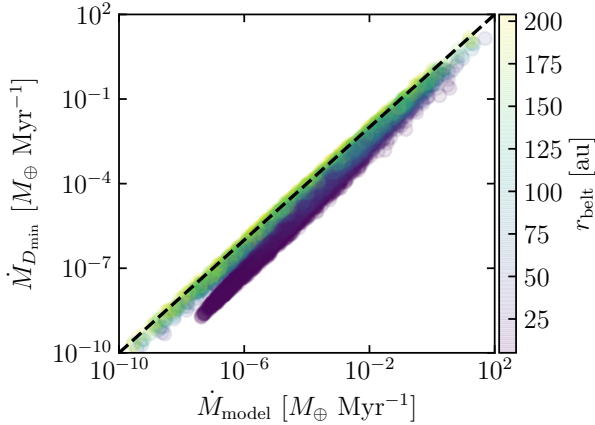


Figure 13. Mass loss rate used in our modelling based on planetesimal parameters and total mass (x axis) vs mass loss rate derived from our model fractional luminosity as in [Matrà et al. \(2017b, y axis\)](#). Each circle corresponds to a different simulation presented in §3.1, and are colour coded according to their belt radius, with purple circles representing small belts and yellow circles large belts. The dashed line represents the $y=x$ curve, i.e. points along the dashed line have consistent mass loss rates.

magnitude smaller due to the large cross section of ionized species, and therefore we estimate that for surface densities larger than $\sim 10^{-17} M_{\oplus} \text{ au}^{-2}$ our treatment is valid. This surface density is much lower than the typical gas surface densities of shielded discs ($\gtrsim 10^{-7} M_{\oplus} \text{ au}^{-2}$) and the unshielded gas discs detected around A stars ($M_{\text{gas}} > 10^{-5} M_{\oplus}$). Only for the lower tail of the population distribution of surface densities around A stars (see Figure 4), the mean free path of molecules and atoms could be comparable or larger than H and thus the evolution of those discs with extreme low gas masses must be taken with caution. Note that this critical surface density is not very sensitive to the choice of H since l is proportional to H .

6 CONCLUSIONS

In this paper we have presented a new numerical model to explain the presence of gas found around nearby young stars with debris discs, with an emphasis on A stars. This gas originates in the interior of planetesimals, and mutual collisions release both dust and gas. Our model (§2) solves for the viscous evolution of the gas (CO, carbon and oxygen) in 1D as it is released by planetesimals (in the form of CO), taking into account the CO photodissociation, self-shielding and shielding by neutral carbon. Our model has one significant addition compared to previous work, it takes into account the time dependent gas release rate due to the disc collisional evolution.

With this model we found that the present gas mass of a disc is highly dependant on the assumed initial disc mass in the form of planetesimals. A system with a constant gas input rate can have a gas mass orders of magnitude lower compared to a system that started with a higher mass and collisionally evolved to an equal planetesimal disc mass. Be-

cause of the nature of collisional evolution of planetesimal discs, dust levels do not depend strongly on the initial disc mass and therefore it is a degenerate problem to try to infer the initial disc mass from dust levels. This means that while a disc might contain low quantities of dust in a collisionally evolved disc, it might have a massive gas disc due to a large initial disc mass. These considerations must be taken into account when analysing gas observations and comparing it with dust levels. However, if CO is unshielded, its short lifetime (~ 120 yr) means that its mass will be set by the present mass loss rate. Conversely, atomic carbon has a longer lifetime as it will viscously evolve on longer timescales which will depend on the kinematic viscosity.

We used this new numerical code to produce the first population synthesis model for exocometary gas around A stars. Population synthesis studies are ideal to deal with degenerate problems and provide constraints on population properties rather than individual systems. Informed by previous studies that fit the dust evolution, we generated samples of 10^4 stars hosting planetesimal discs with random radius, mass and stellar properties. We evolved these systems up to a random age between 3–100 Myr and compare the final distribution to the observed distribution by applying the same selection filters to our model population. We found that our model can reproduce the distribution of CO masses well when viscosities are high ($\alpha \approx 0.1$), even producing a bimodal distribution with a large population of unshielded CO discs and a small fraction of shielded ones. The shielded population is nevertheless common in our models among systems with bright debris discs, which explains why shielded discs are common among the sample of 17 A stars with bright and cold debris discs. The high α value implies that gas needs to be lost on timescales of ~ 1 –10 Myr. Otherwise, carbon readily accumulates shielding CO and producing a large population of shielded and massive CO discs, even around systems with low planetesimal disc masses, which is inconsistent with observations.

Although we focused on A stars, we also tested our model against observations of FGK stars. While massive and shielded CO gas discs are found around A stars, observations of FGK stars have showed that these have low CO gas masses, with only a few detections. Using our model we showed that this is consistent with the collisional evolution studies of discs around FGK stars compared to A stars. Their lower initial disc masses means that gas release rates are lower. Our model quantitatively shows that massive CO gas discs should be very rare around FGK stars if they have similar viscosity levels compared to A stars.

An important test of viscous evolution models of gas in debris discs, is whether gas is observed to extend inwards and accrete onto the star. In §5 we discussed recent observations of neutral carbon around a few systems which seem to indicate that carbon has not spread inwards forming an accretion disc as expected in a viscous evolution scenario. This might suggest that either gas release started recently or is lost through another mechanism, e.g. radiation pressure. Nevertheless, our modelling constrains the gas loss timescale to be ~ 1 –10 Myr (viscous timescale), which could provide insights into alternative mass loss mechanisms. More resolved observations of carbon are needed to conclude.

A potential explanation for the observed cavities in the distribution of carbon could be the presence of planets. A

planet orbiting the system interior to the planetesimal belt could block the inward flow of gas if more massive than $\gtrsim 50 M_{\oplus}$, accreting most of the exocometary gas flowing in. In this scenario, the gas distribution and dynamics could provide constraints on the mass and location of planets at tens of au and interior to massive planetesimal belts.

Finally, we also discussed if gas could affect the dynamics of dust grains. We found that dust should not be heavily affected by gas drag. Only small sub- μm grains that are unbound due to radiation pressure could feel a strong gas drag that could slow their unbound trajectories. However, we find that the predicted gas densities could be high enough to make μm -sized grains to effectively migrate out on timescales comparable to their collisional timescales.

ACKNOWLEDGEMENTS

We thank Richard Booth for valuable input and advice in setting up the numerical code to solve for the viscous evolution of gas considering multiple species. We also thank the anonymous referee for a constructive and thorough review. T.H. acknowledges support from the European Research Council under the Horizon 2020 Framework Program via the ERC Advanced Grant Origins 83 24 28. L.M. acknowledges support from the Smithsonian Institution as a Submillimeter Array (SMA) Fellow.

REFERENCES

- Bath G. T., Pringle J. E., 1981, *MNRAS*, **194**, 967
- Benz W., Asphaug E., 1999, *Icarus*, **142**, 5
- Beust H., Morbidelli A., 1996, *Icarus*, **120**, 358
- Beust H., Vidal-Madjar A., Ferlet R., Lagrange-Henri A. M., 1990, *A&A*, **236**, 202
- Bhowmik T., et al., 2019, arXiv e-prints, p. arXiv:1908.08511
- Booth M., et al., 2013, *MNRAS*, **428**, 1263
- Booth R. A., Clarke C. J., Madhusudhan N., Ilee J. D., 2017, *MNRAS*, **469**, 3994
- Booth M., et al., 2019, *MNRAS*, **482**, 3443
- Bouret J. C., Deleuil M., Lanz T., Roberge A., Lecavelier des Etangs A., Vidal-Madjar A., 2002, *A&A*, **390**, 1049
- Bovy J., 2017, *MNRAS*, **470**, 1360
- Bowler B. P., Nielsen E. L., 2018, Occurrence Rates from Direct Imaging Surveys. p. 155, doi:10.1007/978-3-319-55333-7_155
- Burns J. A., Lamy P. L., Soter S., 1979, *Icarus*, **40**, 1
- Cataldi G., et al., 2014, *A&A*, **563**, A66
- Cataldi G., et al., 2018, *ApJ*, **861**, 72
- Cataldi G., et al., 2019, arXiv e-prints,
- Cavallius M., Cataldi G., Brandeker A., Olofsson G., Larsson B., Liseau R., 2019, arXiv e-prints, p. arXiv:1906.11106
- Crida A., Morbidelli A., Masset F., 2006, *Icarus*, **181**, 587
- Deleuil M., et al., 2001, *ApJ*, **557**, L67
- Dent W. R. F., et al., 2014, *Science*, **343**, 1490
- Dominik C., Decin G., 2003, *ApJ*, **598**, 626
- Draine B. T., 1978, *ApJS*, **36**, 595
- Ferlet R., Vidal-Madjar A., Hobbs L. M., 1987, *A&A*, **185**, 267
- Fernández R., Brandeker A., Wu Y., 2006, *ApJ*, **643**, 509
- Flaherty K. M., et al., 2016, *ApJ*, **818**, 97
- Greaves J. S., et al., 2016, *MNRAS*, **461**, 3910
- Grigorieva A., Thébault P., Artymowicz P., Brandeker A., 2007, *A&A*, **475**, 755
- Hales A. S., Gorti U., Carpenter J. M., Hughes M., Flaherty K., 2019, *ApJ*, **878**, 113
- Higuchi A. E., et al., 2017, *ApJ*, **839**, L14
- Higuchi A. E., et al., 2019, arXiv e-prints, p. arXiv:1908.07032
- Hudson R. D., 1971, *Reviews of Geophysics and Space Physics*, **9**, 305
- Hughes A. M., Wilner D. J., Andrews S. M., Qi C., Hogerheijde M. R., 2011, *The Astrophysical Journal*, **727**, 85
- Hughes A. M., et al., 2017, *ApJ*, **839**, 86
- Iglesias D., et al., 2018, *MNRAS*, **480**, 488
- Kains N., Wyatt M. C., Greaves J. S., 2011, *MNRAS*, **414**, 2486
- Kennedy G. M., Marino S., Matrà L., Panić O., Wilner D., Wyatt M. C., Yelverton B., 2018, *MNRAS*, **475**, 4924
- Kiefer F., Lecavelier des Etangs A., Boissier J., Vidal-Madjar A., Beust H., Lagrange A.-M., Hébrard G., Ferlet R., 2014, *Nature*, **514**, 462
- Kóspál Á., et al., 2013, *ApJ*, **776**, 77
- Kral Q., Latter H., 2016, *MNRAS*, **461**, 1614
- Kral Q., Thébault P., Charnoz S., 2013, *A&A*, **558**, A121
- Kral Q., Wyatt M., Carswell R. F., Pringle J. E., Matrà L., Juhász A., 2016, *MNRAS*, **461**, 845
- Kral Q., Matrà L., Wyatt M. C., Kennedy G. M., 2017, *MNRAS*, **469**, 521
- Kral Q., Marino S., Wyatt M. C., Kama M., Matrà L., 2019, *MNRAS*, **489**, 3670
- Krivov A. V., Löhne T., Sremčević M., 2006, *A&A*, **455**, 509
- Krivov A. V., Ide A., Löhne T., Johansen A., Blum J., 2018, *MNRAS*, **474**, 2564
- Kuiper R., Hosokawa T., 2018, *A&A*, **616**, A101
- Lecavelier Des Etangs A., Vidal-Madjar A., Ferlet R., 1998, *A&A*, **339**, 477
- Lenz D. D., Ayres T. R., 1992, *PASP*, **104**, 1104
- Lieman-Sifry J., Hughes A. M., Carpenter J. M., Gorti U., Hales A., Flaherty K. M., 2016, *ApJ*, **828**, 25
- Löhne T., Krivov A. V., Rodmann J., 2008, *ApJ*, **673**, 1123
- Lubow S. H., D'Angelo G., 2006, *ApJ*, **641**, 526
- Lubow S. H., Seibert M., Artymowicz P., 1999, *ApJ*, **526**, 1001
- Lynden-Bell D., Pringle J. E., 1974, *MNRAS*, **168**, 603
- Lyra W., Kuchner M., 2013, *Nature*, **499**, 184
- MacGregor M. A., et al., 2018, *ApJ*, **869**, 75
- Machida M. N., Kokubo E., Inutsuka S.-I., Matsumoto T., 2010, *MNRAS*, **405**, 1227
- Marino S., et al., 2016, *MNRAS*, **460**, 2933
- Marino S., et al., 2017, *MNRAS*, **465**, 2595
- Marino S., et al., 2018, *MNRAS*, **479**, 5423
- Marino S., Yelverton B., Booth M., Faramaz V., Kennedy G. M., Matrà L., Wyatt M. C., 2019, *MNRAS*, **484**, 1257
- Matrà L., et al., 2017a, *MNRAS*, **464**, 1415
- Matrà L., et al., 2017b, *ApJ*, **842**, 9
- Matrà L., Wilner D. J., Öberg K. I., Andrews S. M., Loomis R. A., Wyatt M. C., Dent W. R. F., 2018a, *ApJ*, **853**, 147
- Matrà L., Marino S., Kennedy G. M., Wyatt M. C., Öberg K. I., Wilner D. J., 2018b, *ApJ*, **859**, 72
- Matrà L., Öberg K. I., Wilner D. J., Olofsson J., Bayo A., 2019, *AJ*, **157**, 117
- Metzger B. D., Rafikov R. R., Bochkarev K. V., 2012, *MNRAS*, **423**, 505
- Montgomery S. L., Welsh B. Y., 2012, *PASP*, **124**, 1042
- Moór A., et al., 2011, *ApJ*, **740**, L7
- Moór A., et al., 2015, *ApJ*, **814**, 42
- Moór A., et al., 2017, *ApJ*, **849**, 123
- Moór A., et al., 2019, arXiv e-prints, p. arXiv:1908.09685
- Mordasini C., Alibert Y., Benz W., 2009, *A&A*, **501**, 1139
- Mumma M. J., Charnley S. B., 2011, *ARA&A*, **49**, 471
- Mustill A. J., Wyatt M. C., 2009, *MNRAS*, **399**, 1403
- Öberg K. I., Murray-Clay R., Bergin E. A., 2011, *ApJ*, **743**, L16
- Olofsson J., et al., 2016, *A&A*, **591**, A108
- Pawellek N., Krivov A. V., 2015, *MNRAS*, **454**, 3207
- Pawellek N., Krivov A. V., Marshall J. P., Montesinos B.,

- Ábrahám P., Moór A., Bryden G., Eiroa C., 2014, *ApJ*, **792**, 65
- Rebollido I., et al., 2018, *A&A*, **614**, A3
- Richert A. J. W., Lyra W., Kuchner M. J., 2018, *ApJ*, **856**, 41
- Rieke G. H., et al., 2005, *ApJ*, **620**, 1010
- Riviere-Marichalar P., et al., 2012, *A&A*, **546**, L8
- Roberge A., et al., 2013, *ApJ*, **771**, 69
- Rollins R. P., Rawlings J. M. C., 2012, *MNRAS*, **427**, 2328
- Schneider G., Silverstone M. D., Hines D. C., 2005, *ApJ*, **629**, L117
- Sepulveda A. G., et al., 2019, arXiv e-prints, p. [arXiv:1906.08797](https://arxiv.org/abs/1906.08797)
- Sibthorpe B., Kennedy G. M., Wyatt M. C., Lestrade J. F., Greaves J. S., Matthews B. C., Duchêne G., 2018, *MNRAS*, **475**, 3046
- Slettebak A., 1975, *ApJ*, **197**, 137
- Stevenson D. J., 1990, *ApJ*, **348**, 730
- Su K. Y. L., et al., 2006, *ApJ*, **653**, 675
- Takeuchi T., Artymowicz P., 2001, *ApJ*, **557**, 990
- Tazaki R., Nomura H., 2015, *ApJ*, **799**, 119
- Teague R., Bae J., Bergin E. A., Birnstiel T., Foreman-Mackey D., 2018, *ApJ*, **860**, L12
- Thébault P., Augereau J.-C., 2007, *A&A*, **472**, 169
- Turner N. J., Willacy K., Bryden G., Yorke H. W., 2006, *ApJ*, **639**, 1218
- Visser R., van Dishoeck E. F., Black J. H., 2009, *A&A*, **503**, 323
- Welsh B. Y., Montgomery S. L., 2018, *MNRAS*, **474**, 1515
- Wyatt M. C., 2005, *A&A*, **433**, 1007
- Wyatt M. C., 2008, *ARA&A*, **46**, 339
- Wyatt M. C., Dent W. R. F., 2002, *MNRAS*, **334**, 589
- Wyatt M. C., Smith R., Greaves J. S., Beichman C. A., Bryden G., Lisse C. M., 2007a, *ApJ*, **658**, 569
- Wyatt M. C., Smith R., Su K. Y. L., Rieke G. H., Greaves J. S., Beichman C. A., Bryden G., 2007b, *ApJ*, **663**, 365
- Zuckerman B., Song I., 2012, *ApJ*, **758**, 77
- Zuckerman B., Forveille T., Kastner J. H., 1995, *Nature*, **373**, 494
- van Dishoeck E. F., Black J. H., 1988, *ApJ*, **334**, 771
- van Dishoeck E. F., Jonkheid B., van Hemert M. C., 2006, *Faraday Discussions*, **133**, 231

APPENDIX A: GAS OBSERVATIONS USED IN THIS WORK

In tables [A1](#) and [A2](#) we show the properties of each of the observed systems that were used to compare to our population synthesis model. Table [A1](#) only shows A stars with ages between 10-50 Myr and debris discs that have fractional luminosities between $5 \times 10^{-4} - 0.01$ and dust temperatures below 140 K. Table [A2](#) shows a similar filtered sample, but without an age restriction. Note that there has not been a complete survey for FGK stars with a selection criteria similar to [Moór et al. \(2017\)](#), and thus Table [A2](#) is likely incomplete.

This paper has been typeset from a $\text{\TeX}/\text{\LaTeX}$ file prepared by the author.

Table A1. Properties of A stars with high fractional luminosity discs ($5 \times 10^{-4} - 0.01$), ages ranging between 10-50 Myr and dust temperatures lower than 140 K. The upper limits correspond to 99.7% confidence levels

Name	Age [Myr]	L_{\star} [L_{\odot}]	f_{IR}	r_{belt} [au]	M_{CO} [M_{\oplus}]	M_{C} [M_{\oplus}]	ref
β Pic	23	8.7	2.6×10^{-3}	105	2.8×10^{-5}	1.0×10^{-3}	1, 2
49 Ceti	40	16	7.2×10^{-4}	96	1.4×10^{-4}	4.0×10^{-3}	3, 4
HD 21997	45	9.9	5.6×10^{-4}	106	6×10^{-2}	—	5
HD 32297	30	8.2	5.5×10^{-3}	100	1.3×10^{-3}	3.5×10^{-3}	6, 7, 8, 9
HD 95086	15	6.1	1.4×10^{-3}	204	4.3×10^{-6}	—	10
HD 98363	15	11	1.3×10^{-3}	32*	$< 9.5 \times 10^{-6}$	—	11, 12
HD 109832	15	5.3	5.4×10^{-4}	25*	$< 7. \times 10^{-6}$	—	11, 12
HD 110058	15	5.9	1.4×10^{-3}	50	2.1×10^{-5}	—	7, 11, 13
HD 121191	16	7.2	4.5×10^{-3}	26*	2.7×10^{-3}	—	11
HD 121617	16	17	4.9×10^{-3}	83	1.8×10^{-2}	—	11
HD 131488	16	13	2.2×10^{-3}	84	8.9×10^{-2}	—	11
HD 131835	16	11	2.2×10^{-3}	90	$4. \times 10^{-2}$	3.3×10^{-3}	13, 14, 15, 16
HD 138813	10	17	$6. \times 10^{-4}$	105	7.4×10^{-4}	—	11, 13, 16
HD 143675	16	8.9	6.9×10^{-4}	28*	$< 1.7 \times 10^{-5}$	—	11, 12
HD 145880	16	19	1.7×10^{-3}	70*	$< 2. \times 10^{-5}$	—	11, 12
HD 156623	16	13	3.3×10^{-3}	94	2.5×10^{-3}	—	13, 16
HR 4796	10	26.	4.8×10^{-3}	79	$< 3.7 \times 10^{-6}$	—	19

References used in this table: (1): [Matrà et al. \(2017a\)](#); (2): [Cataldi et al. \(2018\)](#); (3): [Hughes et al. \(2017\)](#); (4): [Higuchi et al. \(2017\)](#); (5): [Kóspál et al. \(2013\)](#); (6): [Greaves et al. \(2016\)](#); (7): [Kral et al. \(2017\)](#); (8): [MacGregor et al. \(2018\)](#); (9): [Cataldi et al. \(2019\)](#); (10): [Booth et al. \(2019\)](#); (11): [Moór et al. \(2017\)](#); (12): upper limits derived in this work; (13): [Lieman-Sifry et al. \(2016\)](#); (14): [Moór et al. \(2015\)](#); (15): [Kral et al. \(2019\)](#); (16) [Hales et al. \(2019\)](#); (17): [Kennedy et al. \(2018\)](#). ★: The belt radius is calculated as $r_{\text{BB}} \times 1.7$.

Table A2. Properties of FGK stars with high fractional luminosity discs ($5 \times 10^{-4} - 0.01$), with dust temperatures lower than 140 K and without age restrictions. The upper limits correspond to 99.7% confidence levels.

Name	Age [Myr]	L_{\star} [L_{\odot}]	f_{IR}	r_{belt} [au]	M_{CO} [M_{\oplus}]	ref
HD 61005	40	0.7	2.3×10^{-3}	66	$< 6. \times 10^{-6}$	1, 2, 3
HD 92945	100-300	0.37	6.6×10^{-4}	87	$< 3 \times 10^{-5}$	4
HD 107146	80-200	1.0	8.6×10^{-4}	89	$< 5 \times 10^{-6}$	5
HD 111520	15	3.0	1.1×10^{-3}	96	$< 3 \times 10^{-4}$	2, 3, 6
HD 145560	16	3.2	2.1×10^{-3}	88	$< 2 \times 10^{-4}$	2, 3, 6
HD 146181	16	2.6	2.2×10^{-3}	93	$< 3 \times 10^{-4}$	2, 3, 6
HD 146897	10.	3.1	8.2×10^{-3}	81	2.1×10^{-4}	6, 7
HD 170773	1500	3.6	5.0×10^{-4}	193	$< 1.4 \times 10^{-5}$	8
HD 181327	23	2.9	2.1×10^{-3}	86	2.1×10^{-6}	9

References used in this table: (1): [Olofsson et al. \(2016\)](#); (2) [Matrà et al. \(2019\)](#); (3): upper limit and mass derived in this work; (4) [Marino et al. \(2019\)](#); (5): [Marino et al. \(2018\)](#); (6): [Lieman-Sifry et al. \(2016\)](#); (7): [Kral et al. \(2017\)](#); (8) [Sepulveda et al. \(2019\)](#); (9) [Marino et al. \(2016\)](#).